Elsevier Editorial System(tm) for Journal of Power Sources

Manuscript Draft

Manuscript Number: POWER-D-20-00490R2

Title: Experimental and Numerical Study on Catalyst Layer of Polymer Electrolyte Membrane Fuel Cell Prepared with Diverse Drying Methods

Article Type: Research Paper

Keywords: Freeze-drying; Sublimation; Microporous electrode; Mass transport; PEMFC; Drying catalyst layer

Corresponding Author: Mr. Krishan Talukdar, Msc.

Corresponding Author's Institution: German Aerospace Center (DLR)

First Author: Krishan Talukdar, Msc.

Order of Authors: Krishan Talukdar, Msc.; Md Asaduzzaman Ripan, MSc; Thomas Jahnke, PhD; Pawel Gazdzicki, PhD; Tobias Morawietz; Andreas K Friedrich, Professor

Abstract: High manufacturing cost is a major challenge to commercialization of the polymer electrolyte membrane fuel cell (PEMFC) technology in high volume market. Catalyst layer (CL) of PEMFC should incorporate high effective porosity, electrochemically active surface-area, gas permeability, and favorable ionomer distribution. Drying of the CL is a very significant step of electrode fabrication, and determines most of the properties mentioned above, but is rarely a subject of investigation. From various possible drying processes of CL, freeze-drying shows some beneficial properties, such as higher porosity, better ionomer distribution, and reduces the mass transport resistance significantly by allowing more reactant gas into reactive interface. In this work, the influence of diverse drying techniques on the microstructure and performance is investigated. Complementarily, a transient 2D physical continuum-model is used to investigate the effect of the structural properties on cell performance of electrodes prepared with different drying methods. A sensitivity analysis has been also performed to determine the influence of individual parameters applied in the model. Both of the experimental and simulation results stress on the fact that the freeze-drying technique not only significantly enhances the oxygen transport properties through ionomer but also improves the porosity along with the tortuosity of the CL microstructure.

Editor
Journal of Power Sources,
Elsevier.

April 3rd, 2020

Dear Professor Marian Chatenet,

Thank you for reconsidering our manuscript with a minor revision. We would like to express our gratitude to you and the respected reviewers to deliver effort and time in this manuscript. Particularly, we appreciate the positive feedback from the reviewer 2.

We would like to resubmit our manuscript: *"Experimental and Numerical Study on Catalyst Layer of Polymer Electrolyte Membrane Fuel Cell Prepared with Diverse Drying Methods*" to the Journal of Power Sources as a revised version. The corresponding author of this manuscript is I, Krishan Talukdar, and the co-authors are Md Asaduzzaman Ripan, Dr. Thomas Jahnke, Dr. Pawel Gazdzicki, Tobias Morawietz, and Prof. Dr. K. Andreas Friedrich. We would highly appreciate if you accept our revised manuscript with the responses to the "minor revisions" of the reviewer to publish in your Journal.

We have addressed all the issues recommended by the reviewer 2 (marked by red).

In addition to a few typos, we also added more information to make some discussions more understandable to the readers (marked by blue).

The additional modifications are as follows:

Introduction:	Section 1	Page - 5
Materials and Methods:	Section 2.1.1	Page - 8
	Section 2.1.4	Page - 13
	Section 2.1.5	Page - 13, 16
Results and Discussion:	Section 3.1	Page - 22, 23, 24, 25, 26, 31

With the resubmission of this manuscript we undertake the assurance that the above mentioned manuscript consists of original, unpublished work and has not been submitted to any other journal for review.

Sincerely,
Krishan Talukdar
German Aerospace Center (DLR)
Institute of Engineering Thermodynamics
Pfaffenwaldring 38-40, 70569 Stuttgart, Germany

***Response to Reviewers**

Reviewers' comments:

Reviewer #2: The reviewer thanks the authors for answering all the comments/remarks from the first review process.

This reviewer is not totally convince by the explanation given by the authors as to why the porosimetry data from this manuscript is so close to the previous manuscript. There are multiple examples of paper in the literature that have shown that that as the I/C ratio is increased typically the BET, total pore volume and porosity decreases (independent of the type of Carbon support used VC vs. Ketjen black and the technique used to prepare the CL (doctor blade, screen printing, pulse swirl).

But after all the changes done by the authors, the manuscript is now acceptable for publication.

We appreciate your positive comments and important suggestions in the peer review process, and would like to thank you again for your time to review our manuscript once again.

Please fix the following:

In Table 3, for the anode and cathode pressure, please specify if you are 1.5bar Gauge or absolute.

We used 1.5 bar absolute pressure in our experiments. It is now mentioned inside Table 3 : Page 24, Section 2.1.5 .

Through the manuscript change Air to air (not capital A)

The word “Air” changed to “air” in Table 3 : Page 24, Section 2.1.5 .

Figure caption for figure to: c) 1 mA cm-2 should be change to c) 1000 mA cm-2

Figure caption has been corrected to 1000 mA cm^{-2} in Figure 2c): Page 24, Section 3.1.

Finally, we would like to express our gratitude to your kind effort and time all along. The valuable suggestions will improve the quality of the manuscript, and make it more understandable to the readers.

Graphical Abstract

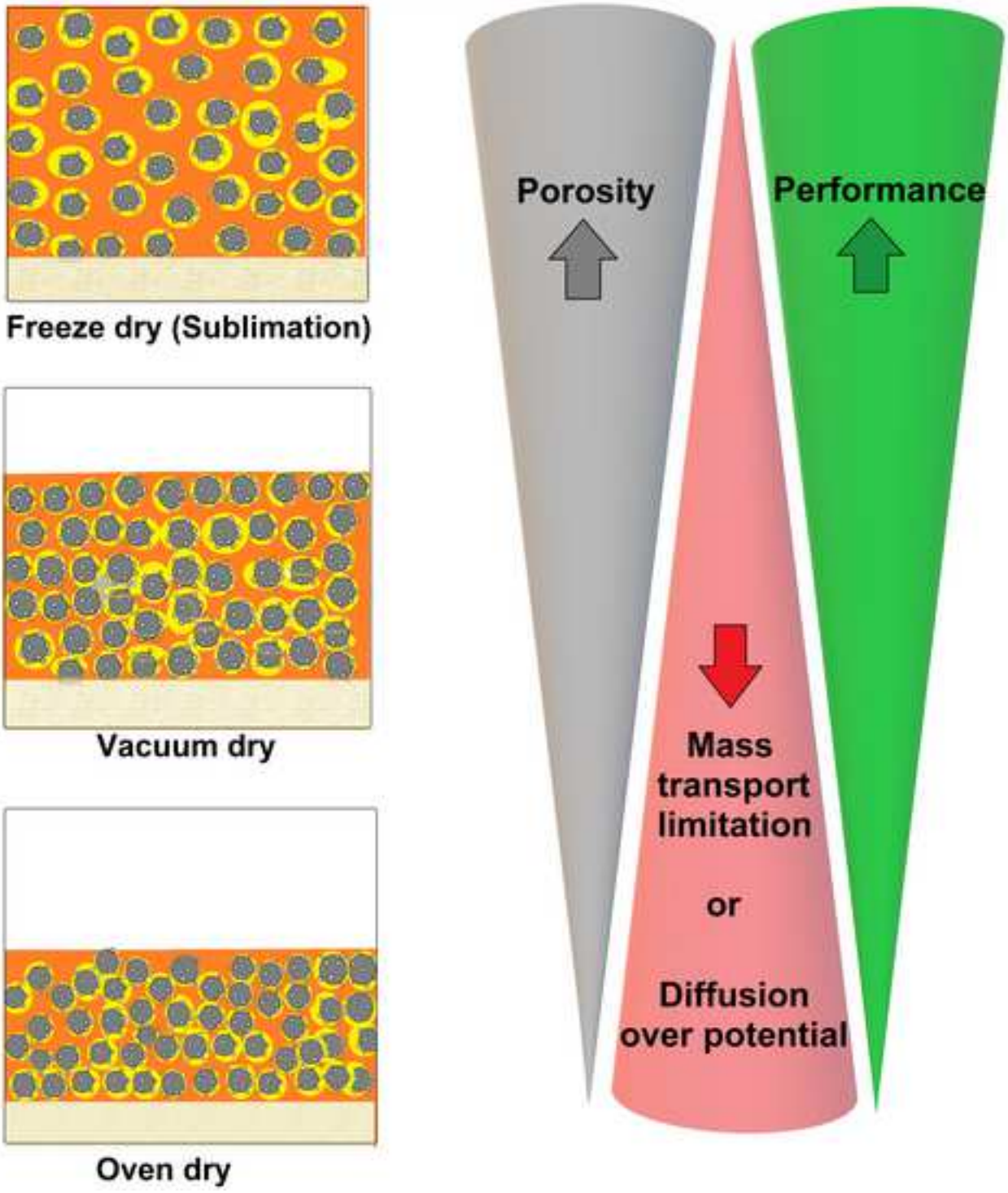

Highlights

- Sublimation significantly improves catalyst layer porosity & ionomer distribution
- Higher ECSA and improved diffusion properties enhance the cell performance
- Simulation deduces an optimized oxygen transport resistance through ionomer film
- Both experimental & simulation results acknowledge improvement due to sublimation

Experimental and Numerical Study on Catalyst Layer of Polymer Electrolyte Membrane Fuel Cell Prepared with Diverse Drying Methods

Krishan Talukdar[1], *Md Asaduzzaman Ripan*[1], *Thomas Jahnke*[1] *Pawel Gazdzicki*[1], *Tobias Morawietz*[1,2], *K. Andreas Friedrich*[1,2]

[1]German Aerospace Center (DLR), Institute of Engineering Thermodynamics, Pfaffenwaldring 38-40, 70569 Stuttgart, Germany

[2]University of Stuttgart, Institute of Building Energetics, Thermal Engineering and Energy Storage (IGTE), Pfaffenwaldring 31, 70569 Stuttgart, Germany

ABSTRACT

High manufacturing cost is a major challenge to commercialization of the polymer electrolyte membrane fuel cell (PEMFC) technology in high volume market. Catalyst layer (CL) of PEMFC should incorporate high effective porosity, electrochemically active surface-area, gas permeability, and favorable ionomer distribution. Drying of the CL is a very significant step of electrode fabrication, and determines most of the properties mentioned above, but is rarely a subject of investigation. From various possible drying processes of CL, freeze-drying shows some beneficial properties, such as higher porosity, better ionomer distribution, and reduces the

mass transport resistance significantly by allowing more reactant gas into reactive interface. In this work, the influence of diverse drying techniques on the microstructure and performance is investigated. Complementarily, a transient 2D physical continuum-model is used to investigate the effect of the structural properties on cell performance of electrodes prepared with different drying methods. A sensitivity analysis has been also performed to determine the influence of individual parameters applied in the model. Both of the experimental and simulation results stress on the fact that the freeze-drying technique not only significantly enhances the oxygen transport properties through ionomer but also improves the porosity along with the tortuosity of the CL microstructure.

KEYWORDS: Freeze-drying, Sublimation, Microporous electrode, Mass transport, PEMFC, Drying catalyst layer

1. INTRODUCTION

Our current energy-intensive lifestyles and population growth makes it difficult to ascertain energy supply and power generation capacity without unacceptable consequences for climate and pollution exposure. There is no doubt that polymer electrolyte membrane fuel cells (PEMFC) with their fast start-up time, high efficiency, sustained operational capacity at high power density, low weighted feature and smooth way of converting chemical energy into electrical energy can be considered as a readily available alternative power source to replace combustion engines running on fossil fuels. Apart from the high cost of the fuel cell stacks and insufficient durability under real conditions, the performance is a major concern especially at low Pt loadings. The microstructure of cathode CL must be carefully investigated considering the rate of irreversible losses in cell voltage is higher in the cathode CL whereas the rate is relatively smaller in the anode CL [1–3].

Microstructure of the catalyst layer and its porosity contributes significantly to the overall measured transport resistance. Excellent dispersion of catalyst particles, high surface area of catalyst support, homogeneously distributed thin ionomer films, favorable network between catalyst-ionomer facilitate better utilization of the catalyst and limit losses through mass and charge transport. Moreover, poor control of humidification within the membrane electrode assembly (MEA) can cause substantial loss in potential. Excess water can prevent reactant diffusion to the catalyst sites by flooding of the electrodes, gas diffusion backings, or flow channels if the water removal is inadequate. An optimized balance between porosity and thickness is required to improve the transport properties like mass transport diffusion electric as well as proton conductivity through the electrodes and precise water management [4–6]. Effective diffusivity, tortuosity, hydrophobicity and pore distribution through gas diffusion layer

(GDL) along with micro porous layer (MPL) are involved in the relation between diffusion media and the performance of PEMFC. The diffusion media also play a significant role in water management with 2-phase liquid and vapor flow [7,8].

Limited utilization of catalyst and endurance of CL is related to its heterogeneous microstructure. Carbon supported Pt and perflurosulfonic acid polymer (predominantly Nafion®) are widely used to fabricate efficient electrode [9–11]. The porous structure of catalyst layer exhibits a wide spectrum of length scales, which covers from 3 to 10 nm of carbon-supported catalyst particles to the Pt/VC agglomerates of 100 – 300 nm due to the binding effect of ionomer at meso-scale. Furthermore, Pt/VC aggregates are sized 1 - 3 μm at macro-scale, and finally the CL as porous medium exhibits a through-plane thickness of 5 – 50 μm. In addition to micro-pores ($\leq$ 2 nm), meso-pores of 2 -20 nm exists within agglomerates. While the agglomerates coalesce into the aggregates, macro or secondary pores network is forged in the crevices. This heterogeneity of electrode porous structure causes imbalanced distribution of porosity and ionomer. Thus it affects both electron and proton conductivity. The interaction between the catalyst particles and ionomer plays a vital role to form efficient reactive interface which is also known as triple phase boundary (TPB). Notably, the different pore sizes and structures dominate the distribution of ionomer and diffusion co-efficient, which in turn influences the performance and durability of electrodes. Moreover, the materialized microstructure after coating and drying technique has a significant impact on water sorption and retention properties of CL which also affects critically into the performance and degradation of the electrode [12–16]. Hence, the importance of consolidating the FC performance with high microporosity or application of high-surface area supports has to be further investigated. CL fabrication is a very important process, and designing a low platinum loaded efficient electrode

with durable performance requires a thin and porous coating, where the catalyst particles and ionomer are homogenously distributed with high surface area. The crucial factors of the fabrication technique are i) ink composition (catalyst/ionomer/solvent ratio), ii) coating techniques (spray / casting / printing or deposition), and iii) drying of the suspension or ink (evaporation / sublimation of the solvent). The final process step, which is drying step, is immensely consequential to obtain a proper and optimized microstructure of the CL.

The paper focusses on properties of catalyst layer structure of PEM fuel cell (PEMFC). Specifically, the impact of the drying step of the catalyst layer (CL) preparation on structure of the CL is studied. Even though it has significant influence on the PEMFC performance, it has not yet fully received attention from the PEMFC community. We have used freeze–drying as a drying technique for low Pt loading electrode fabrication for PEMFC which has been reported recently [15]. The effect of higher porosity and better catalyst utilization in the catalytic layer are obvious from the former study, but the sensitivities of the drying procedure with regarding catalytic layer composition remain unclear. In this work, we have increased the catalyst loading as well as ionomer ratio to intensify the effect of freeze drying on performance as well as electric properties, and simulate the performance with a 2D model. The major characteristic of freeze-drying is the removal of solvent by sublimation from solids without sedimentation. Therefore, freeze-drying of CL prepared from suspension stimulates the porosity of the layer and the corresponding diffusivity. Also ionomer distribution is thought to be more homogeneous. Thickness of the catalyst layer can also be controlled by regulating the catalyst ink composition in this drying method [17]. In this way, it does not only enhance the effective porosity and the electrochemical surface area but also reduce the ionomer resistance inside the CL by distribution of homogeneous ionomer network [17–19]. Moreover, this technique can be adapted to other

electrochemical devices also where porous network plays a significant role in the performance [15,20,21]. It is calculated by several groups that oxygen transport resistance through the ionomer coating on Pt/VC agglomerates is a dominant factor controlling rate determining step of the cathode CL activity at operating FC conditions. It is also proposed that limitations in the transport of oxygen through the ionomer can be offset by reducing the thickness of the ionomer film, and increasing the CL thickness. However, increasing the porosity of the catalyst layer by fabricating thicker catalyst layer and reducing the ionomer thickness decreases the effective proton conductance of the CL [22]. This results inadequate proton conductivity and non-uniform overpotentials in the CL leading to performance losses. Under this scenario, increasing the permeability of oxygen in the ionomer would serve an effective strategy for maintaining fuel cell performance under reduced Pt loading [23,24].

In this study, we have fabricated catalyst layers with same catalyst loading by means of screen printing technique. However, different drying methods (freeze drying, vacuum drying and oven drying) have been applied to the individual CLs to examine the effect of drying techniques into the microstructure of electrodes. Consequently, three different types of MEAs were produced consisting of different cathode CL thickness and architectures, which is reflected in their performance. To correlate their inherent microstructure yielded from distinctive drying methods, with their individual electrochemical properties, physical structural characterizations (focus ion beam scanning electron microscope and atomic force microscope) were also performed. Alongside the experimental works, numerical modeling and simulations are being conducted to get further insight into the performance limitations of the designed electrodes. So many PEMFC models are available now regarding the microstructural phenomenon of electrodes [25–28]. For these simulations a previously developed PEMFC performance model is used which is

implemented in the DLR in-house modeling Framework NEOPARD-X based on Dumu^x [2,29]. is model is used to simulate the cell performance with the three different electrodes and to identify the origin of the improved performance using freeze–drying.

MATERIALS AND METHODS

2.1 Experimental method

The experimental section presents technical information on (i) ink formulations, (ii) applied coating, (iii) drying techniques, (iv) physical characterization methods. (v) MEA fabrication, and (vi) electrochemical characterization methods.

2.1.1 *Ink formulation*

Since the research work is merely focused on the design and development of the cathode side electrode, a commercial GDE was used at the anode side for MEA fabrication. The materials, used for the ink formulation, are listed in Table 1. Three materials are fundamental to formulate a catalyst ink recipe: a catalyst with support, an ionomer and solvent(s). Different solvents such as Tetrahydrofuran (THF), n-butyl acetate, Ethylene glycol were tested before selecting Cyclohexanol as the most promising one to prepare suitable ink for screen-printing method [15].

Table 1: Specification of the ink formulation for screen-printing coating method.

Platinum on Carbon black (40 wt.% Pt/VC)	HiSPEC 4000 Powder	0.5 g	Ionomer to Catalyst powder (Pt/VC) mass ratio is 40:60 [30] or Ionomer to carbon (I/C) ratio is 1.13
Ultra-Pure water HPLC grade	Alfa Aesar	3.0 g	
Cyclohexanol 99%	Sigma-Aldrich	4.0 g	
10 wt.% Solubilized Nafion®	Ion Power	3.4 g	

The ratio between Nafion® ionomer and the total solid particles was kept as 40:60, which can be also expressed as Ionomer carbon ratio: 1.13. We have used higher ionomer-carbon ratio than our previous work [15] (0.69) due to an expected positive effect of freeze drying at higher ionomer contents. Since freeze drying leads to higher porosity we can expect that the catalytic layer can integrate more ionomer without pore blocking but with improved ionic conductivity. We have experienced that the effect of freeze drying is significant when we have higher ratio of ionomer in the catalyst ink. The process of preparation started with weighting the Pt/VC inside a glass beaker and then adding the water in it. Next step is to sonicate the sample on an ELSER– 60 Hz for 30 minutes at a room temperature bath. Afterwards, 10 wt.% Nafion® ionomer was added dropwise using a micropipette. The solution was mixed simultaneously using the bath sonication step for 30 minutes again. As the last component, Cyclohexanol, which must be kept inside a regular oven for 5 minutes at 40° C (melting point of Cyclohexanol is 23° C) to liquify it before using, was added with the mixture. Later, the mixture was sonicated again for 30 minutes like previously mentioned and for 30 minute using 50 Hz (UP200S Hielscher) probe ultrasonicator with 20-50 amplitude and 0.5 cycles. Eventually, the sample was transferred to a ball mill container, which is made of stainless steel (interior container is made of zirconia), and

0.005 mm and 2 mm zirconia balls were used to ball-mill. The suspension was milled at three different rotation speeds of 200, 400 and 1100 rotation per minute (rpm) for 30 cycles. A running cycle for 200 rpm and 400 rpm were 10 minutes with 15 minutes break time between two cycles, whereas a running cycle for 1100 rpm was 5 minutes with 20 minutes break time between two cycles. Three different rpms were applied aiming towards the homogeneous mixing and size reduction of the final particles.

2.1.2 *Coating*

Catalyst coated membrane (CCM) has been fabricated with screen printing technology. For screen-printing coatings, Nafion® XL membranes were cut into squares (6.5 cm x 6.5 cm) and coated in an Aurel 9000 screen-printer coupled with a Koenen polyester mesh with 25 cm^2 opening area (FL-190 10-20 µm EOM). The printing pressure was set to 2.0 $N \cdot cm^{-2}$ and the substrate were kept in place with a vacuum positioning system. The loading of Pt in all CCMs is 0.3 ± 0.02 mg cm^{-2} in each CCM, which was controlled with 3 passes (pre-optimized) of simultaneous screen printing.

2.1.3 *Drying techniques*

After casting with screen-printing, three different drying techniques were applied to different electrodes. These techniques are explained elaborately as following.

Oven Drying: In this technique, a regular laboratory oven was used and the process of drying started with implementing the sample (catalyst coated membrane) inside the oven. The dryer includes ventilation facility along with heat supply. Evaporation occurs at 70 °C and at atmospheric pressure. The sample was kept inside the oven for approximately 12 hours.

Vacuum Drying: The methodology relies on the reduced vapor pressure conditions, which leads to faster evaporation rate at lower temperatures than the boiling point of the solvent. The dryer is attached with a membrane pump, and temperature was set to 70° C for the vacuum dryer. The sample was kept inside the dryer for 5 hours.

Freeze Drying: This drying technique consists of three key stages:

a) Freezing: two most important conditions need to be fulfilled while getting an ideal freeze drying result. The conditions are to preserve the initial physical form by freezing of the material, and to ensure that the sample temperature does not cross the melting point of the solvent. Generally, the temperature is maintained well below triple point to achieve total sublimation. The freezing process has been completed in two steps: initially, cooling the CCM with slow freezing rate for 120 minutes in the regular refrigerator, and then fast freezing using liquid nitrogen. Slow freezing rate will contribute to form bigger ice crystals, which will induce the development of macropores on the matrix of the catalyst layer, which attributes to a rapid sublimation [31,32]. Nevertheless, slow freezing secures that there is no drastic change causing dimensional stress with cracks of other defects in the sample. Then, the CCM samples were taken out from the freezer, and being allocated inside a stainless steel frame, ensuring the electrode would remain flat and stretched. Then the SS frames along with the CCMs were moved into a liquid nitrogen filled container and cooled nearly to -150 °C. Subsequently, previously non-solidified solvent formed smaller crystals due to fast freezing.

b) Primary Drying: The CCMs were then inserted inside the chamber to start sublimation. During this stage, sublimation comes into action to remove the solvent from the remaining product. Deep vacuum (0.3 mbar) is achieved with the help of a rotary pump with a cryogenic trap. The duration of this stage depends on the solvent amount, volume of the drying chamber

and the capacity of the pump. Usually, it takes 2 hours for 2 CCMs in a single batch. Heat of sublimation is provided by raising the temperature of the oven very carefully while monitoring the pressure in the drying chamber. Heat of sublimation is the energy required for the solvent molecules to sublimate form solid state to vapor. This energy is provided externally by means of heat. We increase the temperature to 50° C very slowly (approximately 30 min) without sharp increase of pressure in the system. During the sublimation process the pressure increases slowly to 1 mbar and finally starts dropping to the 0.3 mbar again. When the pressure reaches to the original vacuum pressure, the primary drying is complete.

c) Secondary Drying: The solvent molecules which are bound to the product evaporate in this stage. The chamber is heated to 60° C with a heating rate of 4° C per minute to remove the remaining solvent. The entire freeze drying process takes 4 hours. This freeze drying method is easily scalable for mass production of CCMs, as most of the pharmaceutical industries use this technique to dry drugs; moreover food industries use this drying method very frequently also. After the freeze drying we can immediately use to CCM to fabricate MEA.

2.1.4 *Physical Characterization of the CCMs*

FIB-SEM: Samples prepared for Focus-Ion-Beam Scanning Electron Microscopy (FIB-SEM) were cut into 1×1 cm^2 from a CCM. After placing the sample inside the SEM sample holder, the fracture was made by emerging the sample in liquid Nitrogen. The measurements were carried out in 1.5 kV (electron high tension voltage) EHT (for recording image) with a 30 kV FIB probe (for ion milling). The thickness of each cut is 100 nm. A dual beam microscope integrates the features of a field emission scanning electron microscope (FESEM) with a focused Gallium ion beam (FIB) microscope (ZEISS AURIGA).

Atomic Force Microscopy: As AFM a Multimode 8 AFM (Bruker, Karlsruhe) was used. Conductive adhesive tape was used to glue the MEAs samples onto an AFM steel disc and to electrically connect the surface of the sample. Platinum/iridium coated AFM tips (NCHStPt, Nanoworld) were used in tapping mode with additional recorded nano-mechanical information and electronic current which is averaged by a lock-in amplifier (PF-TUNA, Bruker). The 9 μm² measurements were recorded with 768 × 768 pixels at a scan rate of 0.326 Hz. Images with 4 μm² were cropped out of the measured areas. To measure the surface of the CL by AFM, we have prepared the CCM by screen printing over a membrane only with a single pass of catalyst suspension.

Scanning electron microscopy: To observe the cross section of MEAs with scanning electron microscopy (SEM), specimens were prepared by cutting a 1×1 cm^2 from MEAs. After placing the sample inside the SEM sample holder, the fractures were made by emerging the sample into liquid Nitrogen. The measurement was carried out in a Zeiss UltraPlus, providing an electron beam range of 2.0 to 10 kV that allows the analysis of the surface and the cross section of CL.

Porosity: To measure the surface area and porosity properties of the final catalyst powder, a volume of 5 mL of catalyst ink was placed inside three 10 mL glass beakers. The beakers were dried by (i) oven drying, (ii) vacuum drying, and (iii) freeze-drying respectively. 1 g of dried masses with an uncertainty of +/- 10 mg (from each drying technique applied) were then dried again, under vacuum conditions at 60 °C for 3 h, with liquid nitrogen and positioned inside a Sorptomanic 1195 chamber. Brunauer–Emmett–Telle (BET) measurements were performed using the Dollimore/Heal method for surface area determination of the approached catalyst powder blended with ionomer [33]. We are using the adsorption isotherm for BET analysis [34]. Moreover, the porosity is measured from the hysteresis loop between adsorption and desorption

curve. Moreover, the pore size distribution of the catalyst composite was also determined using mercury intrusion porosimetry (MIP) at 25 ºC. Presently, we cannot measure the porosity with BET and MIT directly on the CCM due to insufficient reproducibility.

Additionally, the porosity of the catalyst layer in CCM was determined from the FIB-SEM images using MATLAB. The pixel count and the contrast of the FIB-SEM images were computed by image processing tool to determine the pore distribution. Pore sizes were calculated as the diameter of a circle with area equal to the detected area. Porosity was quantified by adding all the pore area dividing it by the total pixel count of the picture. It is probable that a systematic deviation between different methods to determine the value of porosity exist so that mainly a comparison between drying procedures with one method is discussed.

2.1.5 *Fuel Cell measurement*

MEA and Cell Preparation:

The MEA was prepared by sandwiching the single side coated CCM with a GDL and a commercial GDE (Fuel Cell etc.) without hot-pressing. The GDL was placed on the coated side of the membrane, which is the cathode. The commercial GDE correspond to the anode electrode, which has a high loading to minimize their influence on performance, and is placed to the opposite side of the cathode. In between we used a Nafion XL membrane to fabricate the MEAs.

Table 2: Specification of the materials used to fabricate MEAs for single cell test. ink formulation for screen-printing, and components to assemble

Material Components	Supplier	Specifications	Function
Nafion® XL	DuPont	27.94 µm thickness	Electrolyte, membrane
Commercial gas	Fuel Cells Etc.	0.3 mg cm^{-2} Pt loading	Anode electrode and GDL

diffusion electrode			
Carbon Paper GDL	SGL Carbon GmbH	25 BC non-woven 235 µm thickness	Gas diffusion layer at the cathode side
Ice cube 35 FC-PO 100 **Gaskets**	QuinTech	2× Frame (1.3 cm width), 5×5 cm^2, 0.5 mm thickness	Sealing
Bipolar plates	DLR	Gold coated SS single channel serpentine flow filed	Cell assembly, Gas distribution
Platinum on Carbon (40 wt.% Pt/VC)	HiSPEC 4000 Powder	Vulcan carbon support	Cathode Catalyst
Ultra-Pure water HPLC grade	Alfa Aesar		Solvent for cathode catalyst ink
Cyclohexanol 99%	Sigma-Aldrich		Solvent for cathode catalyst ink
10 wt.% Solubilized Nafion®	Ion Power	Dispersed in water Eq. wt 1100	Ionomer of the cathode catalyst layer

Two gold coated stainless-still bipolar-plates were used as a flow-field as well as current collector. The area of the flow field is 25 cm^2. The GDLs and GDEs were cut exactly same size of the active area, which means 25 cm^2. A single channel serpentine flow field was used with 1 mm channel width, 1 mm rib width and 0.8 mm depth of channel. 4 pieces 7 mm screws were used with 3 Nm torque. One of the most important factors in the assembly of PEMFCs is to set the appropriate normal compressive stress to the cell to balance the conflicting demands of mitigating gas leaks and decreasing contact resistance without damaging the porous components so that optimal performance is obtained. The amount of compression on the GDL affects the contact resistance, the GDL porosity, and the fraction of the pores occupied by liquid water, which, in turn, affect the performance of a PEM fuel cell [35–38]. In our experiment, we have 17-19 % compression in gas diffusion media while operating the cell in bipolar plate after

clamping. The materials and the operating conditions are stated in Table 2 and Table 3 respectively.

Table 3: Operating parameters for single cell test bench and the model simulator, (*) the minimum flow was maintained for the test station was for the current density 100 mA cm^{-2}.

Parameters	**Symbol**	**100 %RH**	**70 % RH**
Anode stoichiometry* (H_2)	λ_{an}	1.8	1.8
Cathode stoichiometry* (air)	λ_{ca}	2.7	2.7
Cell temperature	T_{cell}	80° C	80° C
Humidifier temperature	$T_{bubbler}$	80° C	70° C
Anode outlet pressure (absolute)	P_{an}	1.5 bar	1.5 bar
Cathode outlet pressure (absolute)	P_{ca}	1.5 bar	1.5 bar

Fuel cell testing condition: The MEAs for single cell characterization were tested in an in-house developed test bench. In our test bench, we have two bubbler humidifiers for both anode and cathode gas inlet; moreover the pressure of the system is regulated after the cell. We have very minute pressure drop before the cell (anode: 5 mbar and cathode: 10 mbar). The operating conditions of the experiment are stated in Table 3. We started to test each MEA with 100 % RH (relative humidity) and subsequently with 70 % RH. The stoichiometry of the cathode and anode were slightly increased to 2.5 and 1.7 with regard to former studies (where 2 and 1.5 was used) to avoid the flooding issue caused by higher ionomer content. 1.5 bar pressure is maintained in fuel cell experiments. It is expected that this changes will lead to an intensification of the performances of the MEAs prepared by different drying methods.

2.1.6 *Electrochemical Characterization of the CCMs*

Break-in and polarization curve: Each MEA was conditioned for 6 hours in 250, 500 and 1000 mA cm^{-2} current density gradually. Break-in step is considered completed if the voltage and current has a stable status (where the voltage change is lower than 10 mV/ hr). Polarization curve was recorded using a Zentro Elektrik electrical load in galvanostatic mode. The cell voltage was monitored as function of the current density with a dwell time of 3 min and with increments of 25 mA cm^{-2} (range: 0 to 100 mA cm^{-2}) followed by steps of 100 mA cm^{-2} (range: 100 mA cm^{-2} to until cell voltage drops to ~200 mV.

Electrochemical impedance spectroscopy (EIS): At normal operating condition, EIS was performed by means of galvanostatic mode using Zahner IM6 potentiostat. EIS spectra were recorded at 100 mA cm^{-2}, 500 mA cm^{-2} and 1000 mA cm^{-2} in the frequency range 100 mHz - 100 kHz with a perturbation amplitude of 5 to 25 mA cm^{-2}, respectively. These measurements were done at both 100 % and 70 % relative humidity with a stoichiometric flow of H_2 and air. Additionally, ionic conductivity (IC) through the CL was measured at a potential of 1 V (potentiostatic mode) [39], using 100 % humidified H_2 and N_2 gases passing through the anode and cathode, respectively (both 100 $mL \cdot min^{-1}$) with a constant flow. Ionic conductivity was measured also in 100 % RH for all MEAs. The applied frequency range was 500 mHz -100 kHz with a perturbation amplitude of 10 mV [40]. Impedance spectra were measured with SIM function of the Zahner software (Thales). All the EIS measurement was performed at 80 °C and 1.5 bar pressure. After adjusting the voltage or current, we have waited 10 mins to perform EIS for ensuring coherent response. Moreover, 3 sets of spectra were recorded to verify the reproducibility of the EIS.

Moreover, Cyclic voltammetry (CV) of the cathode CL was measured in the potential range from 0.06 to 1 V at 80 °C cell temperature using fully humidified (100 % RH) H_2 and N_2 gases passing through the anode and cathode component, respectively with a constant flow rates of both 100 mL min^{-1} [41][42]. Three consecutive CVs were recorded each time and the 2nd CV was considered. For each MEA two sets of CV measurement were performed, and the presented CV is the average of subsequent 2nd CVs from each set. H2 desorption peak were considered to calculate the Pt ECSA of the cathode electrode [43].

2.2 Numerical method

The physical model, which has been used to conduct the research work, is an in-house model implemented in the NEOPARD-X framework [29]. This model includes:

- A 2D along-the-channel geometry with nine spatially resolved layers (anode and cathode channels, GDLs, MPLs, CLs and the membrane)
- A multiphase Darcy model for the two-phase, multicomponent transport within the porous electrodes
- Butler-Volmer kinetics for the ORR and HOR reactions
- Energy transport through all layers of the cell
- A membrane model including coupled water and proton transport as well as transport of dissolved gas species
- Proton transport through the ionomer within the CLs and electron transport through the support phase of the porous electrodes
- An ionomer film model describing the oxygen transport from the gas phase through the ionomer film to the cathode catalyst

All corresponding model equations are discussed in detail in [29]. In the following, only the modeling aspects most relevant for this work are summarized. Diffusion in the porous electrode is described by the Stefan-Maxwell equation [44]

$$\nabla x_\alpha^i = \sum_{j=1}^{N} \frac{C_\alpha^i C_\alpha^j}{C_\alpha^2 D_{eff,\alpha}^i} \left(\frac{d_\alpha^j}{C_\alpha^j} - \frac{d_\alpha^i}{C_\alpha^i} \right), \tag{3.2}$$

where C_α^i and C_α^j are the molar concentration of species *i* and *j* in phase α, and consecutively d_α^i and d_α^j represent diffusive flux density of species *i* and *j* in phase α. $D_{eff,\alpha}^\kappa$ is the effective diffusion coefficient, which is calculated based on a binary diffusion coefficient, D_α^κ. The effect of porous media is taken into account by Bruggemann-correction of the diffusion coefficients

$$D_{pm,\alpha}^\kappa = (\phi S_\alpha)^{1.5} D_\alpha^\kappa \,, \tag{3.3}$$

where ϕ is the porosity and S_α is the saturation of phase α. In the gas phase, Knudsen diffusion occurs and $D_{eff,\alpha}^\kappa$ is calculated with a Bosanquet approximation,

$$D_{eff,g}^\kappa = \left(\frac{1}{D_{pm,g}^\kappa} + \frac{1}{D_{Knudsen,g}^\kappa} \right)^{-1} \tag{3.5}$$

with

$$D_{Knudsen,g}^\kappa = r_{pore} \frac{2}{3} \sqrt{\frac{8RT}{\pi M^\kappa}} \tag{3.6}$$

Here, $D_{Knudsen,g}^\kappa$ represents the Knudsen diffusion coefficient of component κ in gas phase, M^κ denotes the molar mass of component κ; *R, T* and r_{pore} express ideal gas constant, temperature and pore radius respectively. Proton transport through the CL is described by Ohm's law

$$\Psi^{H^+} = -\sigma_{eff}^{H^+} \nabla \Phi_{ion} \tag{3.8}$$

The amount of water activity plays a vital role in proton conductivity. A material-dependent empirical relation has been implemented to describe the influence of water activity on proton conductivity $\sigma_{eff,CL}^{H^+}$. An exponential dependence on the water activity [45] has been defined as,

$$\sigma_{eff,CL}^{H^+}(a^{H_2O}) = A \times \exp\left(Ba^{H_2O}\right) \tag{3.9}$$

Where A and B are fitting parameters. The volumetric reaction rate of Oxygen Reduction Reaction (ORR) is calculated using an ionomer film model

$$r^{ORR} = \frac{-R\kappa^{ORR} + \sqrt{4ECSA_{eff}^2 n^2 F^2 c_g^{O_2} + R^2\left(\kappa^{ORR}\right)^2}}{2\, n\, F\, ECSA_{eff}}\ \kappa^{ORR} \tag{3.10}$$

r^{ORR} =Volumetric reaction rate of ORR, R =Lumped ionomer resistance, κ^{ORR} =Rate constant of ORR, $ECSA_{eff}$ =Effective electrochemically active surface area n= Number of transferred electrons, F= Faraday's constant, $c_g^{O_2}$= Molar concentration of oxygen. This model takes into account the oxygen transport resistance through the ionomer film,

$$R = R_{diff} + R_{int} \tag{3.11}$$

which consists of the resistance due to the oxygen diffusion through the ionomer film

$$R_{diff} = \frac{\delta_{ion}}{D_{ion}} \tag{3.12}$$

and the water activity dependent interfacial resistance which is described by the empirical relation

$$R_{int} = C \exp\left(Da^{\mathrm{H_2O}}\right). \tag{3.13}$$

All the parameters applied in this model as well as relevant to this study are mentioned in the **result and discussion** as table 4 and 5.

3 RESULTS AND DISCUSSION

3.1. *Experimental results:*

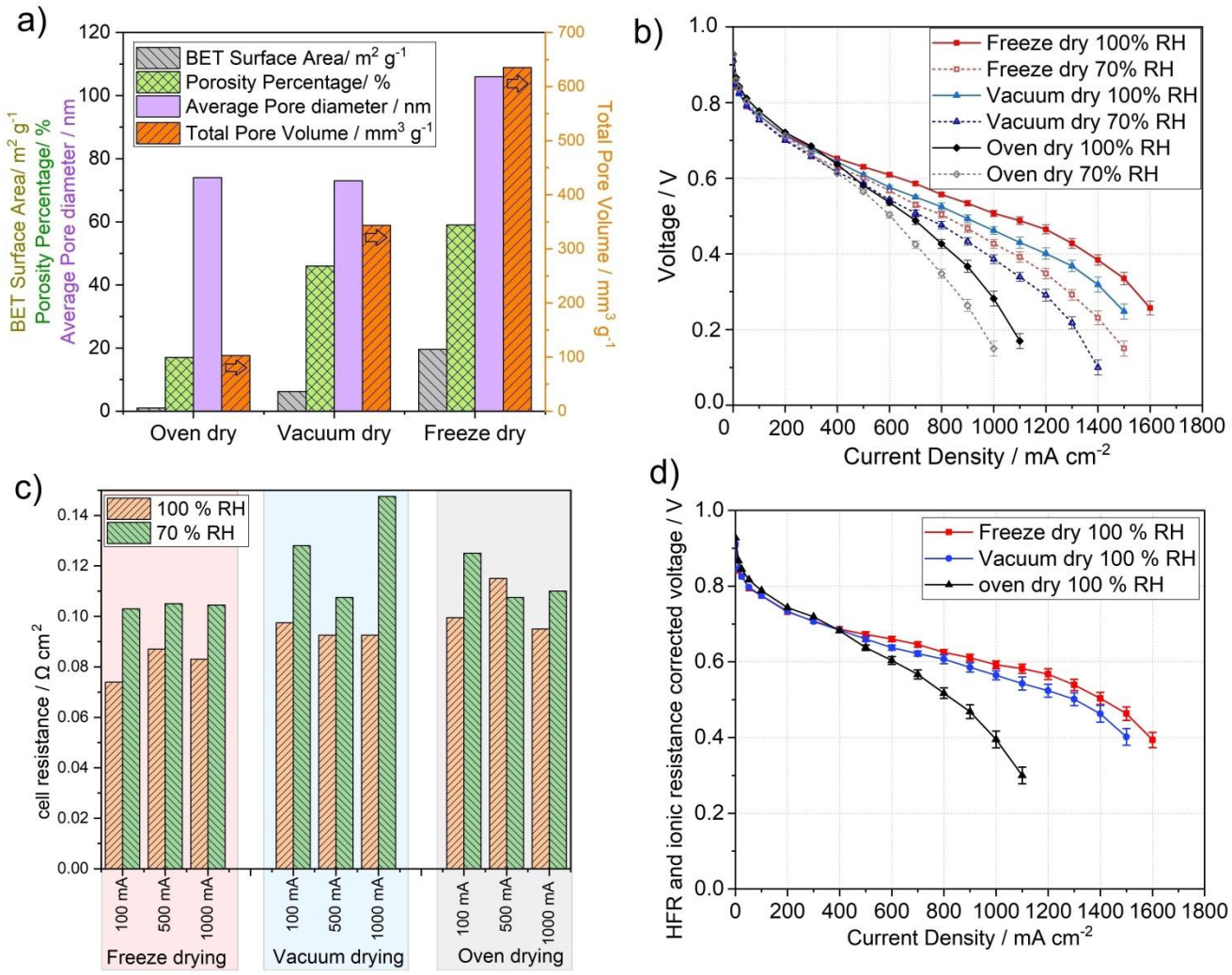

Figure 1: a) Morphological characterization of the free standing (non-coated) Pt/ VC/ Nafion® powder shaped by oven, vacuum and freeze drying method. Left-axis exhibits parameters of BET surface area (Grey), porosity percentage (Green), average pore diameter (Purple) and right-axis graph exhibits parameters of total pore volume (orange); H_2/ air polarization curves of MEAs with freeze, vacuum and oven dried screen-printed cathode catalyst layers with 0.3 mg cm^{-2} Pt loading at 100% RH (relative humidity) and 70% RH. The temperature was 80 °C with

stoichiometric flow and the back pressure was maintained 1.5 bar for both anode and cathode; c) cell ohmic resistance or high frequency resistance (HFR) of three MEAs in different humidification; d) polarization curves with HFR and ionic resistance corrected voltage of the 3 different MEAs in 100 % RH and same condition as Fig 1b).

An experimental study was performed to generate sufficient data to characterize the effect of different drying techniques on the micro and macro structure of the electrode to validate the numerical model. Porosimetry study of the catalyst powder / ionomer derived from three different drying techniques but identical suspension was characterized, and demonstrated in Fig. 1a). However, the unit for the BET surface area and total pore volume are normalized to mass of total powder (Pt/ VC/ Nafion®). According to the BET analysis, freeze drying of the catalyst suspension yields more effective surface area than vacuum drying and oven drying. Since sublimation is the process characteristics of the freeze-drying technique, the development of larger pores is associated to the transition of solid solvent crystals directly to the vapor state, and the result is a wider network of pores. This behavior is also visible in Fig. 1a), where the calculated average pore diameter of the freeze-dried sample is higher than the others. It is assumed that the pore size and pore volume of the cathode catalyst layer increases and the over-potential associated to diffusion of reactants is likely reduced. This reduction of diffusion over-potential is in compliance with the better cell performances as verified by Yim et al. [46]. Moreover, Fischer et al. stated back on 1998 that the additional porosity across the thin film electrodes could also improve the cathode performance, in particular with air as oxidant [47]. Purple bars (3rd column) of the Fig. 1a) demonstrate the numerical value of the average pore diameter of the Pt/ VC/ Nafion® after drying which also follows the same trend. Therefore, it is

evident that the drying step does affect the final micro / macro structure of the catalyst layer and consequently the performance of PEM fuel cell.

All the single cell tests were conducted in a 25 cm^2 active area cell and an in-house built fuel cell test bench. Three sets of experiments were conducted and an average has been used to make the figure of merits. Three CCMs produced via screen-printing technique, were physically and electrochemically characterized. A quantitative performance analysis of PEMFC is characterized by a polarization curve or I-V (current voltage characteristics) curve. The polarization curve is plotted with the error bars which were calculated from the standard deviation of the 3 independent measurements [36][48]. Please note that these I-V curves are not performed under differential conditions that mean that heterogeneous conditions leads to lower overall performances compared to measurements in differential cells. Fig. 1b) illustrates a relative humidity dependence I-V curve comparison of the MEAs fabricated with three different drying conditions. Each MEA has been tested at 100% RH along with 70% RH. Moreover, Fig. 1d) represents the polarization curves with HFR and ionic resistance (R_{ion}) corrected voltage of the 3 different MEAs in 100 % RH and same condition as Fig 1b). The HRF and R_{ion} corrected voltage $U_{cell,corr}(j) = U_{cell}(j) + (HFR + R_{ion})*j$ is calculated using the average HFR obtained from measured data at 100 mA cm^{-2}, 500 mA cm^{-2} and 1000 mA cm^{-2} and constant values of R_{ion} (see Figure 2d). The open circuit voltage is commonly influenced by electrode electrochemical activity as well as the exchange current density. It is noticeable in Fig. 1b) that the open circuit voltage (OCV) does not depend on the tested RH conditions and the drying technique. This is a consequence of the application of the same catalyst ink and coating technique during the formulation of CCMs. Moreover, the kinetics, the contact resistance, the partial pressure of the reactant gasses and the operating conditions were also indistinguishable in the I-V polarization

curve in all cases. The variance starts at current densities > 400 mA cm^{-2}. Moreover, diffusion loss or mass transfer limitation plays a major role at higher current density. Improved porosity and homogeneous distribution of ionomer network (will be shown in Fig. 3) facilitate the diffusion properties in the reactive interphase [15,49], which in turn reduces the concentration loss. Apparently, at higher current density the voltage loss of oven dried MEA is greater than vacuum dried MEA, and decreases to the lowest in case of freeze dried MEA. The aforementioned phenomenon is supported by a sharp drop of performance in oven dried MEA comparing to the others. The freeze dried MEA shows considerably superior performance; whereas vacuum dried MEA shows medium performance. The poor performance of the oven dried MEA is due to the higher transport limitation and the lower compression capacity of the catalyst layer. This trend is justifiable for both of the relative humidity: RH 100 % and 70 %. Considering that 100 % RH provides more humidity into the cell, and as a consequence yields higher power due to increase proton conductivity of the ionomer leading to lower ohmic resistance of the MEA. The effect of lower relative humidity on performance is more significant for vacuum dried and freeze dried MEA compared to the oven dried MEA. We speculate that this phenomenon is due to the higher porosity of vacuum dried and freeze dried catalyst layer, which leads to a better distribution of ionomer with higher surfaces areas exposed to gas phase. With increasing porosity we expect a simultaneous decrease of ionomer film thickness. Hence, at lower RH the water content of the thinner ionomer film decreases compared to the thicker ionomer film with a concurrent loss of conductivity. This circumstance lowers the performance at 70 % RH in freeze and vacuum dried MEA. Fig 1c) represents the cell ohmic resistance or high frequency resistance (HFR) of three MEAs in different humidification. 70 % RH shows higher resistance comparing to 100% RH due to the lack of water content in the membrane and

electrode assembly, which in turn reduce the ionic conductivity. As will be shown next, it is very likely that also a higher transport resistance arises for thin ionomer films at reduced humidity which exacerbates performance losses at higher current densities.

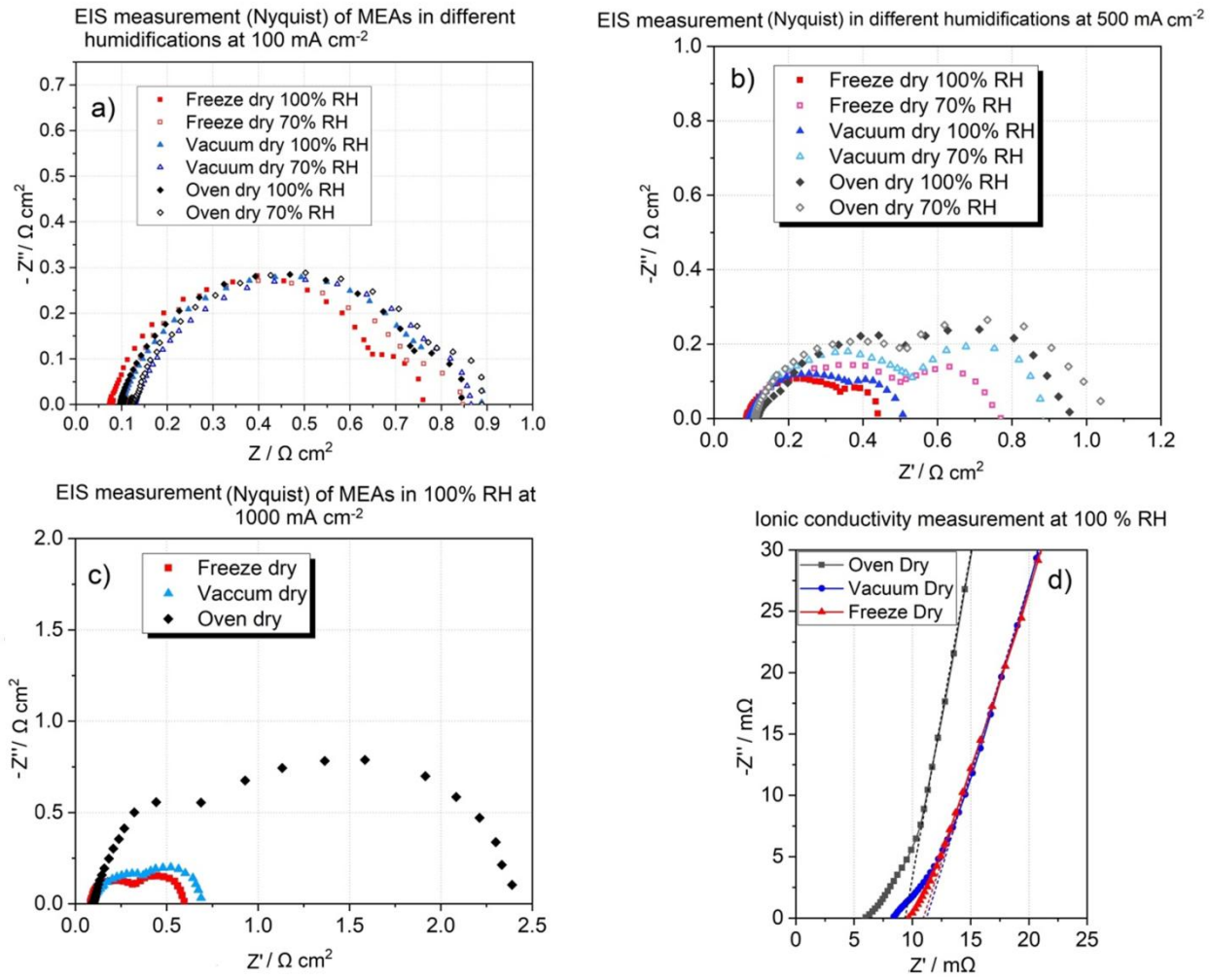

Figure 2: Nyquist Impedance spectra a) 100 mA cm^{-2} at 100% RH and 70% RH for three different CCMs dried in three different ways, b) 500 mA cm^{-2} at 100% RH and 70% RH, c) at 1000 mA cm^{-2} only at 100% RH, d) the ionic impedance measurement of 25 cm^2 MEAs at 100% RH (not area normalized).

A qualitative and quantitative measurement was performed by the Electrochemical Impedance Spectroscopy (EIS). Through the Nyquist plot, individual contributions to the voltage loss are attributed to the particular time constants, which are finally represented according to the distinctive arcs (overlapped semicircles in practice) [50]. High frequency resistance, which is originated from the proton conductivity of the membrane and the resistance (HFR) of the total system, is related to the left side intercepts of the horizontal axis in the Nyquist plot. As all the external parameter of the MEAs are identical, the HFR or the ohmic resistance of the all the MEAs are similar. At the medium frequency region, reaction kinetics contributes, and the first semicircle is attributed to the cathode charge transfer resistance. Fig. 2a) and b) shows a Nyquist plot of the three MEAs at 100 mA cm^{-2} and 500 mA cm^{-2}, respectively, both in 100 % and 70 % relative humidity.

Additionally, Fig. 2c) displays the Nyquist impedance plot at 1000 mA cm^{-2} only in 100 % RH. As the first semicircle is associated with cathode kinetics, the impedance demonstrated in Fig. 2a), b) and 2c) are mainly caused by the charge transfer. From the Fig. 2 a) we can see more or less identical charge transport behavior, which is also consistent with the polarization curve in Fig. 1a). At low current density, the kinetic overpotential of all the MEAs exhibit similar behavior as they were fabricated with same catalyst loading. However, with increasing current density the behavior changes and the process associated to charge transfer for freeze dried and vacuum dried MEA shows smaller semi-circles as compared to oven dried MEA. The charge transfer resistance in Fig. 2 b) and c) of both freeze dried as well as vacuum dried MEAs is relatively comparable. Since, in both cases we see more or less similar type of semi-circle for freeze dried and vacuum dried MEA. On the contrary, oven dried MEA carries much higher charge transport limitation with a much bigger (first) semicircle in both current densities that can

be also deduced from the current voltage curve in Fig. 1b). Besides, due to the significant volume of water generates in the cathode electrode at high current density, significant amount of pores of the CL might get blocked. As a result, without sufficiently available pores, the diffusion of the reactants might get hindered if the water removal is not efficient. Therefore, at higher current densities, optimized porosity and effective water management are the key to minimize mass-transport losses [51]. It is very apparent from the Fig. 2b) and 2c) that oven dried MEA results in a significant mass transport loss presumably due to less porosity and flooding of water, which is demonstrated by the large second semicircle in all the cases. However, the freeze dried MEA and vacuum dried MEA show a moderate mass transport loss owing to its higher porosity and better ionomer network in the catalyst layer [52]. Bigger pore volume and homogeneous ionomer distribution make an efficient water management through the CL, and it reflects over the smaller diffusion semicircle as well as improved performance of freeze dried MEA at high current density. However, it is interesting to note that even for the MEAs with superior porosity the mass transport limitations are exacerbated significantly when reducing humidity. Since it is unlikely that ionic conductivity influences mass transport, this observation is indicative of higher oxygen transport resistance through the ionomer films. Gas transport through membranes is well-known to depend on the water content of the membranes. The significant influence of humidity on the mass transport related process indicates that the ionomer in the catalytic layer shows a similar behavior.

The ionic conductivity measurements of the catalytic layer with H_2 and N_2 (cathode) flow is shown in Fig 2d) with 100 % relative humidity. This EIS measurement is indicative of the proton conductivity through the cathode catalyst layer assuming a transmission line model. Protonic resistance, R_{ionic}, through three differently dried CCLs can be determined from the magnitude of

the Warburg-like region (45°) projected onto the real impedance (Z') axis (=R_{ionic} /3) [53], which were portrayed by dotted lines in Fig 2d). The lowest value of the protonic resistance across the CCL is obtained for the freeze dried electrode (R_{ionic} 4.08 mΩ). On the contrary, the highest protonic resistance is calculated from oven drying CCL (R_{ionic} 9.6 mΩ), followed by the vacuum dried CCL (R_{ionic} 8.4 mΩ). These values are interpreted as signaling a better ionomer distribution associated also to higher performance of the MEAs even though they have lower ECSA (see Fig. 5b). Area normalized values for oven dried, vacuum dried and freeze dried electrodes are 0.24, 0.21 and 0.1 Ω cm^2 respectively.

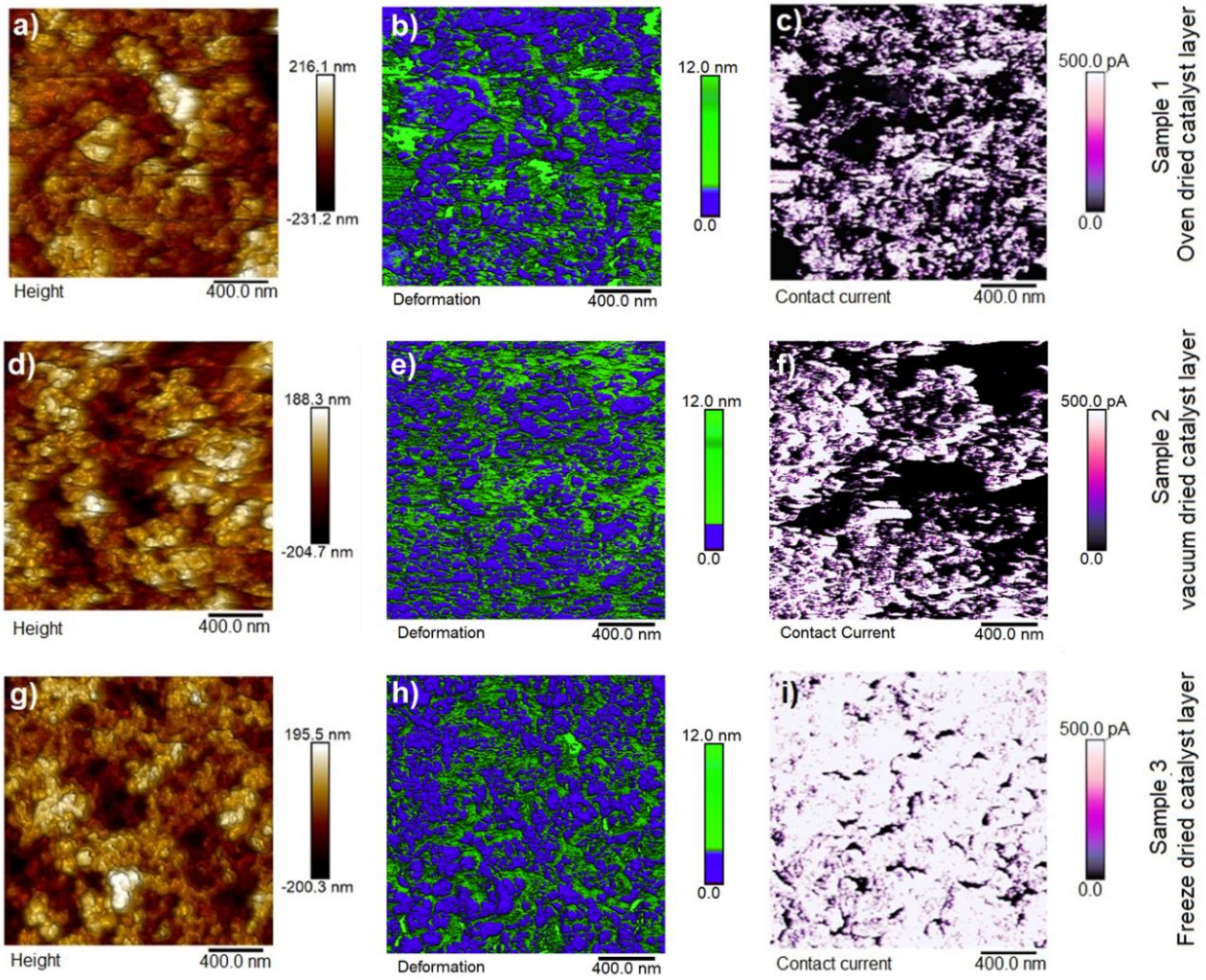

Figure 3: AFM analysis: a/d/g) height/ topography measurement of three different CL, b/e/h) deformation measurement to ionomer detection, c/f/i) electronic current measurement from three different CL by contact current.

The AFM analysis of the different drying techniques on the surface of the CL is shown in Fig. 3. Measurements were conducted with PeakForce Tapping mode with additional recorded current. With this AFM technique one can get the topographical information along with nanoelectrics and nanomechanical properties. The height/topography, deformation and electronic current studies are shown in Fig. 3, whereas a stiffness property is shown in SI Fig. 1. The height model from AFM measurements gives the topography of the samples including the roughness and an impression of the porosity. The stiffness, adhesion (not shown) and deformation information provides clear contrast between Pt/VC and the ionomer in the catalyst layer. The electronic current gives also an insight into the conductive network formed. Additionally, thick ionomer layers can be detected due to no electronic current. Figure 3 a), d) and g) are exhibiting the topographic properties by evaluating the vertical movement of the AFM tip. From the AFM height measurement, oven dried CL illustrates a high amount of catalyst particle agglomerates as visible in the topographic images in Fig. 3-a, whereas vacuum and freeze drying shows better dispersion of catalyst comparing to oven drying in Fig. 3 d), g). Hence, Fig. 3 d), g) suggests a better distribution of particles due to vacuum drying and freeze drying (well distribution of bright color). Nevertheless, integrating the information from adhesion, deformation and current measurement, we can suggest that the freeze dried CL demonstrates smaller catalyst aggregates and their well distribution over the surface. Therefore, even though Sample 2 and 3 look similar from topographic point of view in Fig. 3 d) and g), their conductivity differs significantly as shown by the right hand panels. The adhesion and deformation study provides similar behavior

of ionomer distribution; however, in this article deformation is demonstrated due to having better contrast.

The deformation information along with the electronic current also depicts a high amount of ionomer agglomeration visible in green (high deformation) and no electronic current areas (dark purple). The opposite in the data is true for the catalyst. The vacuum dried CL shows a high amount of ionomer agglomeration as best seen in the electronic current channel, but as well in the stiffness (SI Fig. 1), and the deformation. Nevertheless, the ionomer structure in the non-agglomerate areas are more homogeneous than in oven dried CL. The large ionomer areas might also be a part of the exposed membrane as the electrode was kept very thin. As appeared in the Fig 3g), the freeze dried CL (sample 3) has the most homogeneous structure with highest nanoporosity and lowest agglomeration as visible in the height channel. The ionomer is well distributed between the catalyst particles. This can be seen best in the deformation channel (Fig. 3h) between the green ionomer and the blue catalyst particles. In agreement with Fig. 3i), the ionomer layer thickness might be very small as most of the area is electronically conductive. The force (Peakforce) was kept constant for all measurements.

Three material dependent properties have been determined experimentally to understand the origin of the performance differences for the three drying techniques. The cross-sectional SEM images captured to measure the thickness of the dry electrodes are demonstrated in Fig. 4.

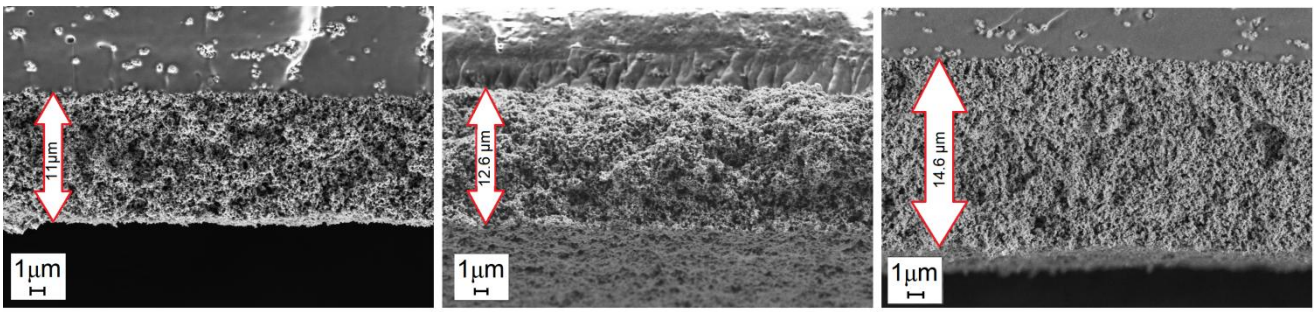

Oven Dry Vacuum Dry Freeze Dry

Figure 4: The SEM images from cross-sections of MEAs prepared with different drying techniques.

Pt ECSA was determined from the H_2 desorption signal from CV, while the porosity was measured by FIB-SEM. A 3D reconstruction of the catalyst layer microstructure has been obtained from a stack of SEM images, each image taken after 100 nm cut by the ion beam. An in-house MATLAB image processing tool was used to calculate the porosity and the pore size distribution from the images by calculating the difference in contrast and the resolution of the image. The porosity of the BET measurement is derived from the powder. However, the porosity will change upon coating the powder on a membrane. Therefore, we tried to implement the more realistic porosity value, and used the porosity data derived from the FIB-SEM analysis of the CCM. Porosity measurement of CL in CCM by BET/ MIP (mercrury intrusion porosimetry) has been performed and reported recently [34][54], however we are still trying to adapt the CCM porosity measurement technique by BET/ MIP in our facility. Fig. 5a) shows the catalyst layer captured by FIB-SEM, and the area of the pores which we counted to measure the porosity and pore diameter distribution. We observe from Fig. 5a) that the numerical porosity of the catalyst layer is also increased from oven dry to freeze dry. The aforementioned values of porosity are very much compliant with the CV measurement of the MEAs. We can see from the Fig 5b) that the freeze dried catalyst layer shows more electrochemically active surface area than the other MEAs. As CL prepared in this study has higher Nafion content when in fact higher ionomer content with inhomogeneous thickness distribution causes some of the Pt particle inaccessible. Therefore the Pt ECSA is smaller than the commonly used CL. A bar chart of calculated Pt ECSA (determined from desorption peak) values is also included as an inset image of Fig. 5b). In this article, we have measured lower ECSA value than expected, and we speculate that the

reason is the higher ionomer content in the catalyst layer used compared to usual preparations. Vulcan is one of the carbon supports for Pt catalyst with reduced micro and meso porosity. Recent publications have shown that the ionomer does not penetrate the micro pores of carbon support; instead in catalyst layer ionomer covers mainly the outside of the carbon support and the aggregates [55][56]. Increasing ionomer content probably increases Pt coverage which has been shown to reduce Pt activity. It is therefore, also plausible that ECSA is reduced, but we have to further analyze the ECSA dependence on ionomer content. Higher surface area of catalyst particles and porosity are responsible for the higher ECSA value of freeze dried MEA. However, vacuum dried MEA shows a moderate ECSA value which is in between oven and freeze drying. The trend of the porosity, CV and ECSA also agrees with the performance of each MEA.

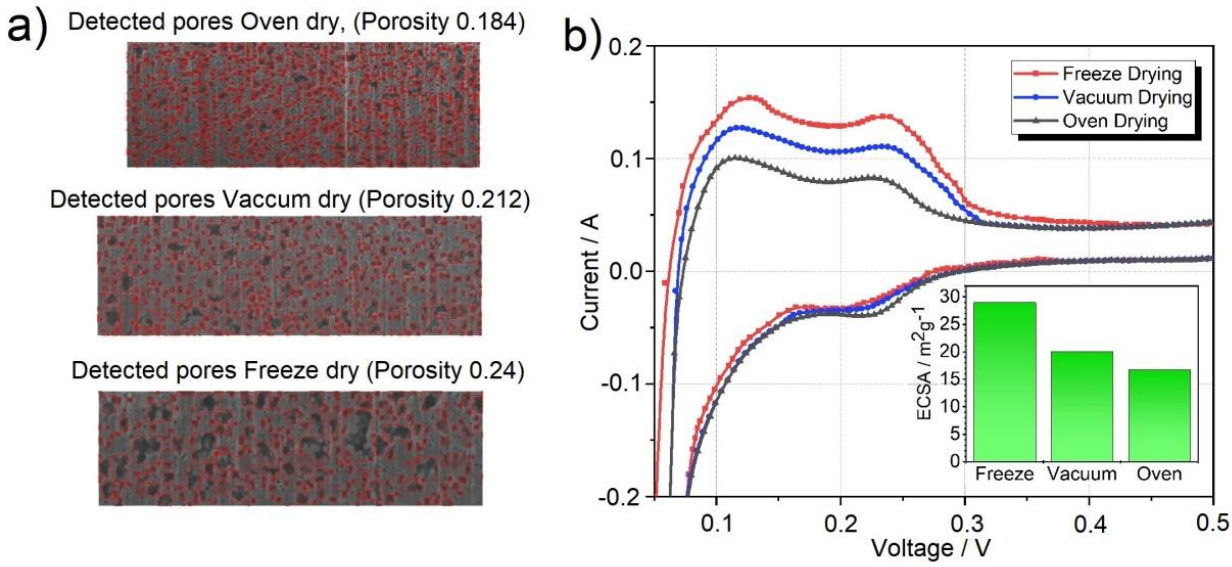

Figure 5: a) FIB-SEM analysis along with MATLAB image processing applied on the image to measure porosity and pore size distribution, b) Cyclic voltammetry measurement of three different drying techniques including the Pt ECSA values (inset of b). These CLs are compressed to fabricate MEAs.

3.2. *Simulation results:*

The main focus of the simulation work is to better understand the origin of the experimentally observed differences in performance for the three CL materials and to explore the variation of performances due to different parameters such as porosity, ECSA and CL's thickness which are likely to have important contributions on the performances. The basic experimental parameters used in numerical model are referred in Table 4.

Table 4: The experimental parameters utilized in the numerical model

	CCL Thickness, m	ECSA, m^2g^{-1}	Porosity, %
Freeze drying	14.58×10^{-6}	29.16	24
Vacuum drying	12.67×10^{-6}	20.28	21
Oven drying	11×10^{-6}	16.61	18

To further investigate the origin of the different performance of the three catalyst layers we have simulated polarization curves at 100 % RH and 70 % RH with the physical model described in the numerical part of the experimental and method section.

The measured values for CL thickness, porosity and ECSA for each material have been used in the respective simulations. The only significant fitting parameters used are the ionic conductivity of the CL and the ionomer film resistance, which are assumed to vary depending on the drying technique due to changes in the microstructure of the CLs. Along with porosity, permeability, CL and ionomer conductivity, some modified spatial and electrochemical parameters, which are also used in the model are mentioned in Table 5. For all other model parameter the values reported in [29] have been used.

Table 5: The model parameters used in the numerical analysis.

MPL (Permeability, porosity and pore diameter)	
$\mathbf{K}_{MPL}$= 4.0×10^{-15} [m^2]	
$\emptyset_{MPL}$= 0.75	
$r_{pore,\,MPL}$= 45×10^{-9} [m]	
Thermal conductivity(GDL, MPL, CL)	
λ_{GDL}= 0.60 [Wm^{-1}k^{-1}]	
λ_{MPL}= 0.33 [Wm^{-1}k^{-1}]	
λ_{CL}= 0.3 [Wm^{-1}k^{-1}]	
Exchange current density (ORR)	
i^{0}_{ref}= 1.0e^{-4} [A m^{-2}]	
CL conductivity	
FD and VD	OD
A= 1.0× 10^{-2} [Sm^{-1}]	A= 0.80 × 10^{-2} [Sm^{-1}]
B= 3.0	B= 3.0
Ionomer film resistance to oxygen transport	
FD and VD	OD
C= 2.5 × 10^{5} [sm^{-1}]	C= 2.2648 × 10^{4} [sm^{-1}]
D= 5.0	D= -1.5

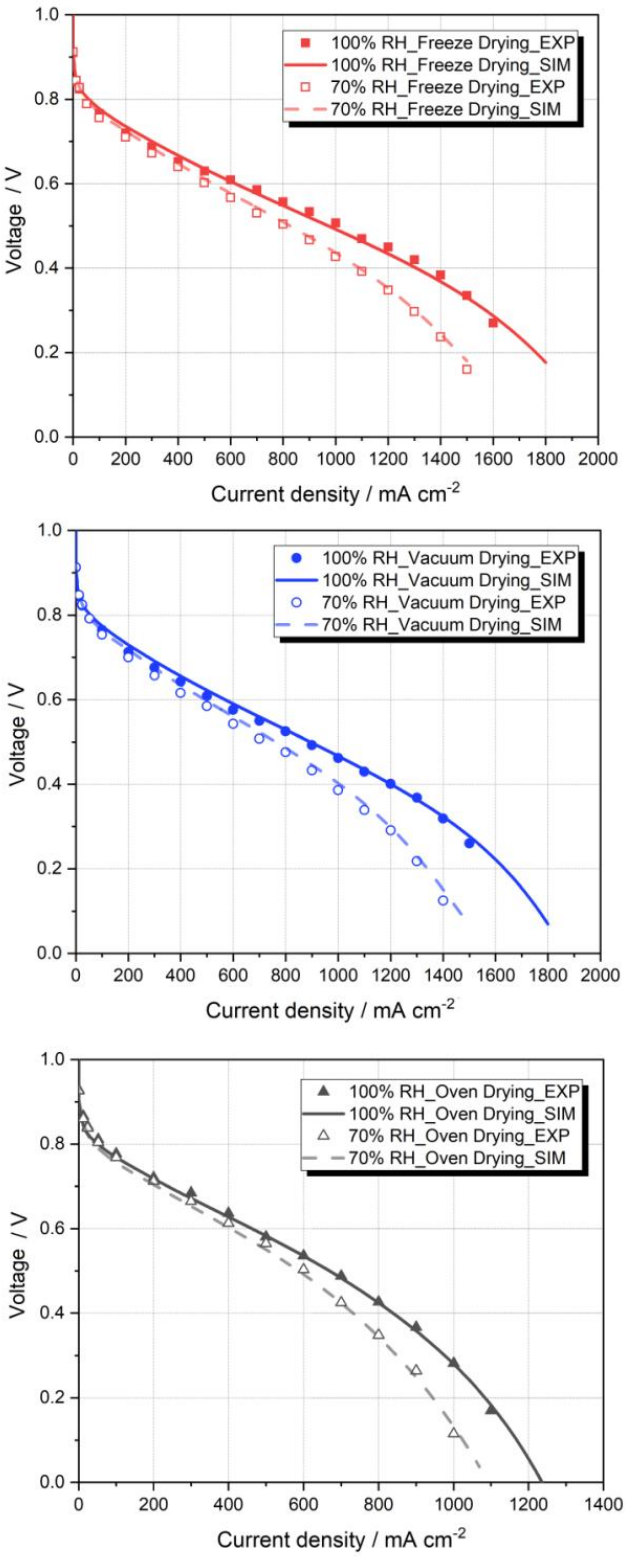

Figure 6: Fitting of the simulation and experimental polarization curves for three different drying techniques in different relative humidity.

Fig. 6 shows the comparison between the simulated and experimentally measured polarization curves. A good agreement is obtained for all the cases, independently to the relative humidity and drying conditions. Interestingly, the same fitting parameters for ionic conductivity and ionomer film resistance were obtained for freeze drying and vacuum drying. This demonstrates that the difference in performance between these two drying techniques can be explained solely by the difference in CL thickness, porosity and ECSA. Instead, for oven drying a significantly higher ionomer film resistance and lower ionic conductivity was obtained which indicates a less favorable ionomer distribution within the CL in this case.

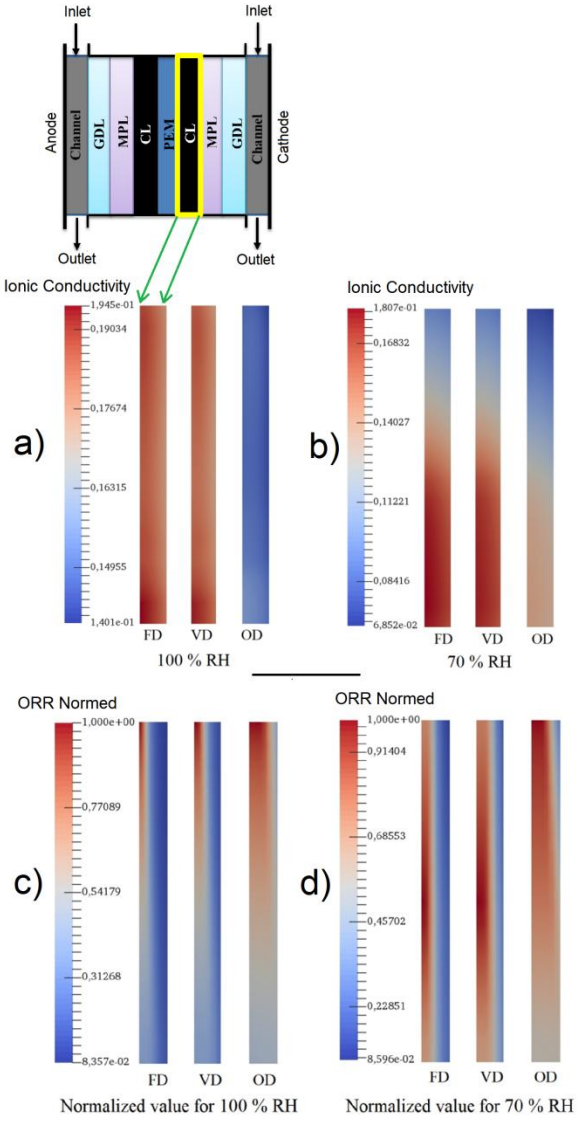

Figure 7: a-b) Ionic conductivity (Sm-1) in CLs due to Freeze drying (FD), Vacuum drying (VD) and Oven drying (OD) techniques in different relative humidity; c-d) ORR rate (Am^{-3}) at 1500 mA cm^{-2} in cathode CLs for freeze drying (FD), vacuum drying (VD) and oven drying (OD) technique for different relative humidity. Normalized values have been plotted to avoid the residual effect of the measurement.

The model also allows studying the local conditions inside cell. Fig. 6a) highlights the distribution of ionic conductivity throughout the catalyst layer. The membrane is on the left and the gas inlet on the top, as shown in the schematic diagram of the model geometry. For visualization purposes the images are scaled by a factor of 10^4 in x-direction. Compared to the freeze dried and vacuum dried catalyst layers, the oven dried MEA yields a poor ionic conductivity in both humidity condition. The drying out of ionomer near the inlet reduces the ionic conductivity for all MEA simulations at 70 % humidification. To get further insight into the difference between the three catalyst layers, Fig. 6b) shows the simulated spatial distribution of the ORR reaction rate within the cathode CL. As one can see, for 100 % RH in case of freeze drying the higher ECSA allows for a higher reaction rate close to the membrane. Instead, for VD and especially for OD the ORR is distributed more homogeneously over the thickness of the CL which introduces additional performance losses due to the low ionic conductivity of the CL. The same holds true for 70 % RH. The main difference is that in case of FD and VD the highest reaction rate shifts from the inlet towards the middle of the cell due to drying out of the ionomer close to the inlet. Instead for OD the highest reaction rate remains close to the inlet, probably due to the lower porosity which reduces the drying out effect.

To perform a sensitivity analysis of the fitting parameter fitting parameters have been altered. The goal is to investigate how the individual changed parameters influence the fitting as well as

outcome of the simulation. To investigate the effect of the three material parameters CL thickness, porosity, ECSA as well as two fitting parameters the ionomer film resistance, ionic conductivity, a sensitivity analysis has been performed in which all of the parameters are varied by +/-25 %. Figure 8 shows the sensitivity analysis effect on the parameters at a current density of 1500 mA cm^{-2}. It can be seen that the ECSA strongly affects the performance especially at 70% RH, while the effect of porosity and CL thickness is minor. Interestingly, a lower porosity leads to slightly lower performance at 100% RH but higher performance at 70% RH. This can be attributed to the counterbalance between reduced oxygen transport through the pores and the reduced drying out of the ionomer at lower porosity. The figure also shows that the cell performance is very sensitive to both fitting parameters, i.e., ionic conductivity and ionomer film resistance especially at lower RH.

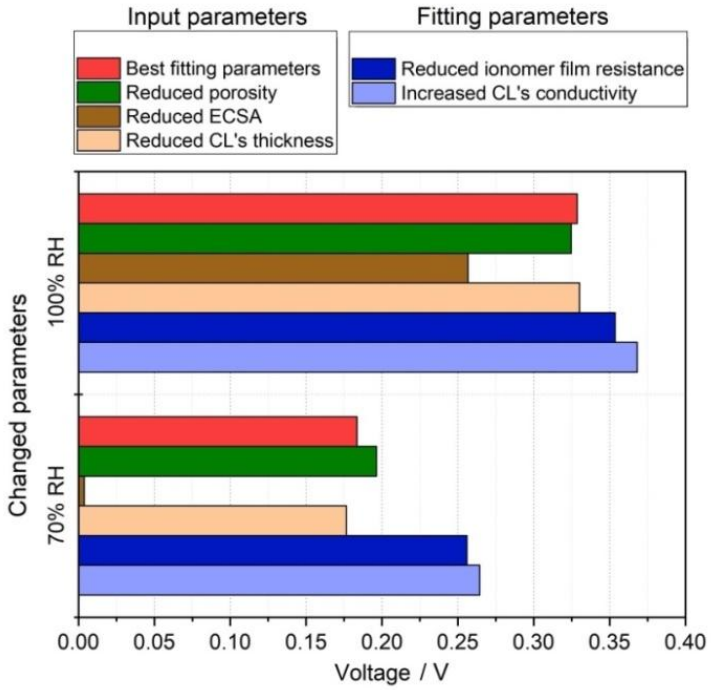

Figure 8: Bar plots emphasizing the influence of input and fitting parameters on the freeze dried MEA (± 25 %) at 1500 mA cm^{-2} in both 100 % and 70 % relative humidity.

4 CONCLUSION

It is demonstrated by our work that the limitations in the transport of oxygen through the ionomer can be negate by optimizing the thickness of ionomer film by different drying methods, and increasing the CL thickness by improving its porosity. However, increased porosity, thicker electrode and very thin ionomer film hamper the charge transport within the CL, which counterbalances the higher permeability and diffusibility of oxidant in the reacting interface. Thus, optimized CL microstructures are needed to minimize both charge and oxygen transport losses. The electrochemical and ex-situ characterizations highlight the improved performance of freeze dried catalyst layer at high current density due to the reduced concentration polarization. This improvement in mass transport and better ionomer distribution is supported by the numerical model we have used in this study. The simulation yields a very good agreement with the experimental results, and the fit accurately explains how the improved oxygen transport behaviour triggers the performance. In summary, from both experimental and numerical points of view, we can stress on the fact that the drying technique plays a major role for the PEMFC performance due to its effect on the distribution and thickness of the ionomer layer through the catalyst layer as well as on the porosity. A well optimized catalyst layer with these above mentioned properties will raise the power density of the PEMFC application.

Nevertheless, systematic durability tests of the freeze dried CL would be the next step. Moreover, investigation of the limiting current density by means of varying oxygen concentration will give a significant clue to perceive the quantitative concentration limitation. Another future prospect is to improve our model of the CL by accommodating the drying effect more deeply, considering the rate of evaporation and rate of deposition along with the thermal conductivity of individual materials.

ACKNOWLEDGEMENT

Krishan Talukdar acknowledges financial support by DAAD. The authors thank Siegfried Graf for building up and maintaining the fuel cell test benches Dr. Noriko Sata for the assistance with porosity measurements, and Julio Cesar Garcia Navarro for his contribution to determine the pore size distribution by MATLAB. Author also wants to acknowledge the kind cooperation of Professor Hermenegildo Garcia and his team from Universitat Politècnica de València for the FIB-SEM measurement. Additionally, the authors appreciate the support of the reviewers in the peer review process; the precise comments as well as critical suggestions helped to improve this manuscript.

REFERENCES

[1] S. Litster, G. McLean, PEM fuel cell electrodes, J. Power Sources. 130 (2004) 61–76. doi:10.1016/j.jpowsour.2003.12.055.

[2] T.E. Springer, M.S. Wilson, S. Gottesfeld, Modeling and Experimental Diagnostics in Polymer Electrolyte Fuel Cells, J. Electrochem. Soc. 140 (2016) 3513–3526. doi:10.1007/978-4-431-56042-5_22.

[3] C. Marr, X. Li, Composition and performance modelling of catalyst layer in a proton exchange membrane fuel cell, J. Power Sources. 77 (1999) 17–27. doi:10.1016/S0378-7753(98)00161-X.

[4] S. Takahashi, T. Mashio, N. Horibe, K. Akizuki, A. Ohma, Analysis of the Microstructure

Formation Process and Its Influence on the Performance of Polymer Electrolyte Fuel-Cell Catalyst Layers, ChemElectroChem. 2 (2015) 1560–1567. doi:10.1002/celc.201500131.

[5] A. Kongkanand, M.F. Mathias, The Priority and Challenge of High-Power Performance of Low-Platinum Proton-Exchange Membrane Fuel Cells, J. Phys. Chem. Lett. 7 (2016) 1127–1137. doi:10.1021/acs.jpclett.6b00216.

[6] V. Mehta, J.S. Cooper, Review and analysis of PEM fuel cell design and manufacturing, J. Power Sources. 114 (2003) 32–53. doi:10.1016/S0378-7753(02)00542-6.

[7] F. Gloaguen, P. Convert, S. Gamburzev, O.A. Velev, S. Srinivasan, An evaluation of the macro-homogeneous and agglomerate model for oxygen reduction in PEMFCs, Electrochim. Acta. 43 (1998) 3767–3772. doi:10.1016/S0013-4686(98)00136-4.

[8] S. Von Kraemer, M. Puchner, P. Jannasch, A. Lundblad, G. Lindbergh, Gas diffusion electrodes and membrane electrode assemblies based on a sulfonated polysulfone for high-temperature PEMFC, J. Electrochem. Soc. 153 (2006). doi:10.1149/1.2335979.

[9] J. Zhao, A. Ozden, S. Shahgaldi, I.E. Alaefour, X. Li, F. Hamdullahpur, Effect of Pt loading and catalyst type on the pore structure of porous electrodes in polymer electrolyte membrane (PEM) fuel cells, Energy. 150 (2018) 69–76. doi:10.1016/j.energy.2018.02.134.

[10] R. O'Hayre, F.B. Prinz, The air/Platinum/Nafion Triple-Phase Boundary: Characteristics, Scaling, and Implications for Fuel Cells, J. Electrochem. Soc. 151 (2004) A756. doi:10.1149/1.1701868.

[11] K. Talukdar, H.J. Kim, Y.H. Kim, H.C. Lee, S.J. Choi, Polyacrylamide/Nafion® semi-

interpenetrating networks as proton-conducting membrane of direct methanol fuel cell, Sci. Adv. Mater. 6 (2014) 2389–2394. doi:10.1166/sam.2014.2190.

[12] T. Soboleva, K. Malek, Z. Xie, T. Navessin, S. Holdcroft, PEMFC catalyst layers: The role of micropores and mesopores on water sorption and fuel cell activity, ACS Appl. Mater. Interfaces. 3 (2011) 1827–1837. doi:10.1021/am200590w.

[13] J. Wang, Formation and Characteristics of Microstructures from PEM Fuel Cell Catalyst Ink Drying, (2015). http://hdl.handle.net/10012/9537.

[14] S.-J. Talukdar, Krishan; Kim, Hee Jin; Kim, Young Ho; Park, Younjin; Lee, Ho-Chang; Choi, Proton-Conducting Membranes from Nafion®/Polystyrene Sulfonate Composite for Fuel Cell Applications, J. Nanoelectron. Optoelectron. 10 (2015) 535–540.

[15] K. Talukdar, S. Delgado, T. Lagarteira, P. Gazdzicki, K.A. Friedrich, Minimizing mass-transport loss in proton exchange membrane fuel cell by freeze-drying of cathode catalyst layers, J. Power Sources. 427 (2019) 309–317. doi:10.1016/j.jpowsour.2019.04.094.

[16] K. Talukdar, S. Helmly, M. Schulze, D.G. Sanchez, M. Handl, R. Hiesgen, J. Kraut, K.A. Friedrich, Enveloping of catalyst powder by ionomer for dry spray coating in polymer electrolyte membrane fuel cells, J. Power Sources. (2019) 82–90. doi:10.1016/j.jpowsour.2019.03.093.

[17] Z. Xia, S. Wang, L. Jiang, H. Sun, F. Qi, J. Jin, G. Sun, Rational design of a highly efficient Pt/graphene-Nafion® composite fuel cell electrode architecture, J. Mater. Chem. A. 3 (2015) 1641–1648. doi:10.1039/c4ta05399k.

[18] W. Abdelwahed, G. Degobert, S. Stainmesse, H. Fessi, Freeze-drying of nanoparticles:

Formulation, process and storage considerations, Adv. Drug Deliv. Rev. 58 (2006) 1688–1713. doi:10.1016/j.addr.2006.09.017.

[19] N. Pramounmat, C.N. Loney, C.O. Kim, L. Wiles, K.E. Ayers, A. Kusoglu, J.N. Renner, Controlling the Distribution of Perfluorinated Sulfonic Acid Ionomer with Elastin-like Polypeptide, ACS Appl. Mater. Interfaces. 11 (2019) 43649–43658. doi:10.1021/acsami.9b11160.

[20] R. Fernández, P. Ferreira-Aparicio, L. Daza, PEMFC electrode preparation: Influence of the solvent composition and evaporation rate on the catalytic layer microstructure, J. Power Sources. 151 (2005) 18–24. doi:10.1016/j.jpowsour.2005.02.048.

[21] H.S. Park, Y.H. Cho, Y.H. Cho, C.R. Jung, J.H. Jang, Y.E. Sung, Performance enhancement of PEMFC through temperature control in catalyst layer fabrication, Electrochim. Acta. 53 (2007) 763–767. doi:10.1016/j.electacta.2007.07.046.

[22] R. Darling, Modeling air electrodes with low platinum loading, J. Electrochem. Soc. 166 (2019) F3058–F3064. doi:10.1149/2.0101907jes.

[23] S. Holdcroft, Fuel cell catalyst layers: A polymer science perspective, Chem. Mater. 26 (2014) 381–393. doi:10.1021/cm401445h.

[24] Y. Tabe, M. Nishino, H. Takamatsu, T. Chikahisa, Effects of cathode catalyst layer structure and properties dominating polymer electrolyte fuel cell performance, J. Electrochem. Soc. 158 (2011) 1246–1254. doi:10.1149/1.3624606.

[25] A.Z. Weber, R.L. Borup, R.M. Darling, P.K. Das, T.J. Dursch, W. Gu, D. Harvey, A. Kusoglu, S. Litster, M.M. Mench, R. Mukundan, J.P. Owejan, J.G. Pharoah, M. Secanell,

I. V. Zenyuk, A critical review of modeling transport phenomena in polymer-electrolyte fuel cells, J. Electrochem. Soc. 161 (2014) F1254–F1299. doi:10.1149/2.0751412jes.

[26] R. Vetter, J.O. Schumacher, Free open reference implementation of a two-phase PEM fuel cell model, Comput. Phys. Commun. 234 (2019) 223–234. doi:10.1016/j.cpc.2018.07.023.

[27] K. Malek, T. Mashio, M. Eikerling, Microstructure of Catalyst Layers in PEM Fuel Cells Redefined: A Computational Approach, Electrocatalysis. 2 (2011) 141–157. doi:10.1007/s12678-011-0047-0.

[28] J. Huang, Z. Li, J. Zhang, Review of characterization and modeling of polymer electrolyte fuel cell catalyst layer: The blessing and curse of ionomer, Front. Energy. 11 (2017) 334–364. doi:10.1007/s11708-017-0490-6.

[29] G.A. Futter, P. Gazdzicki, K.A. Friedrich, A. Latz, T. Jahnke, Physical modeling of polymer-electrolyte membrane fuel cells: Understanding water management and impedance spectra, J. Power Sources. 391 (2018) 148–161. doi:10.1016/j.jpowsour.2018.04.070.

[30] G. Sasikumar, J.W. Ihm, H. Ryu, Optimum Nafion content in PEM fuel cell electrodes, Electrochim. Acta. 50 (2004) 601–605. doi:10.1016/j.electacta.2004.01.126.

[31] M.J. Pikal, S. Shah, D. Senior, J.E. Lang, Physical chemistry of freeze- drying: Measurement of sublimation rates for frozen aqueous solutions by a microbalance technique, J. Pharm. Sci. 72 (1983) 635–650. doi:10.1002/jps.2600720614.

[32] J. Lee, Y. Cheng, Critical freezing rate in freeze drying nanocrystal dispersions, J. Control. Release. 111 (2006) 185–192. doi:10.1016/j.jconrel.2005.12.003.

[33] D. Dollimore, G.R. Heal, An improved method for the calculation of pore size distribution from adsorption data, J. Appl. Chem. 14 (1964) 109–114. doi:10.1002/jctb.5010140302.

[34] T. Soboleva, X. Zhao, K. Malek, Z. Xie, T. Navessin, S. Holdcroft, On the micro-, meso-, and macroporous structures of polymer electrolyte membrane fuel cell catalyst layers, ACS Appl. Mater. Interfaces. 2 (2010) 375–384. doi:10.1021/am900600y.

[35] J. Ge, A. Higier, H. Liu, Effect of gas diffusion layer compression on PEM fuel cell performance, J. Power Sources. 159 (2006) 922–927. doi:10.1016/j.jpowsour.2005.11.069.

[36] M.B. Sassin, Y. Garsany, B.D. Gould, K. Swider-Lyons, Impact of Compressive Stress on MEA Pore Structure and Its Consequence on PEMFC Performance, J. Electrochem. Soc. 163 (2016) F808–F815. doi:10.1149/2.0291608jes.

[37] R.W. Atkinson, Y. Garsany, B.D. Gould, K.E. Swider-Lyons, I. V. Zenyuk, The Role of Compressive Stress on Gas Diffusion Media Morphology and Fuel Cell Performance, ACS Appl. Energy Mater. 1 (2018) 191–201. doi:10.1021/acsaem.7b00077.

[38] C. Simon, F. Hasché, H.A. Gasteiger, Influence of the Gas Diffusion Layer Compression on the Oxygen Transport in PEM Fuel Cells at High Water Saturation Levels, J. Electrochem. Soc. 164 (2017) F591–F599. doi:10.1149/2.0691706jes.

[39] G. Li, P.G. Pickup, Ionic conductivity of PEMFC electrodes effect of Nafion loading, J. Electrochem. Soc. 150 (2003). doi:10.1149/1.1611493.

[40] K. Talukdar, P. Gazdzicki, K.A. Friedrich, Comparative investigation into the performance and durability of long and short side chain ionomers in Polymer Electrolyte

Membrane Fuel Cells, J. Power Sources. 439 (2019).

[41] R. Carter, S. Kocha, F. Wagner, M. Fay, H. Gasteiger, Artifacts in Measuring Electrode Catalyst Area of Fuel Cells through Cyclic Voltammetry, ECS Trans. 11 (2007). doi:10.1149/1.2780954.

[42] K. Cooper, Laboratory #4 – Fuel Crossover by Linear Sweep Voltammetry & Electrochemical Surface Area by Cyclic Voltammetry, (2009) 1–3. doi:10.1533/9781845694838.344.

[43] C. Breitkopf, K. Swider-Lyons, Springer Handbook of Electrochemical Energy, Springer Berlin Heidelberg, 2016. https://books.google.de/books?id=I_qoDQAAQBAJ.

[44] R.B. Bird, W.E. Stewart, E.N. Lightfoot, Transport Phenomena, Wiley, 2006. https://books.google.de/books?id=L5FnNlIaGfcC.

[45] B.P. Setzler, T.F. Fuller, A physics-based impedance model of proton exchange membrane fuel cells exhibiting low-frequency inductive loops, J. Electrochem. Soc. 162 (2015) F519–F530. doi:10.1149/2.0361506jes.

[46] S.D. Yim, Y.J. Sohn, S.H. Park, Y.G. Yoon, G.G. Park, T.H. Yang, C.S. Kim, Fabrication of microstructure controlled cathode catalyst layers and their effect on water management in polymer electrolyte fuel cells, Electrochim. Acta. 56 (2011) 9064–9073. doi:10.1016/j.electacta.2011.05.123.

[47] A. Fischer, J. Jindra, H. Wendt, Porosity and catalyst utilization of thin layer cathodes in air operated PEM-fuel cells, J. Appl. Electrochem. 28 (1998) 277–282. doi:10.1023/A:1003259531775.

[48] C. Simon, F. Hasché, H.A. Gasteiger, Influence of the gas diffusion layer compression on the oxygen transport in PEM fuel cells at high water saturation levels, J. Electrochem. Soc. 164 (2017) F591–F599. doi:10.1149/2.0691706jes.

[49] S. Holdcroft, Fuel cell catalyst layers: A polymer science perspective, Chem. Mater. 26 (2014) 381–393. doi:10.1021/cm401445h.

[50] M. Eikerling, A.A. Kornyshev, Electrochemical impedance of the cathode catalyst layer in polymer electrolyte fuel cells, J. Electroanal. Chem. 475 (1999) 107–123. doi:10.1016/S0022-0728(99)00335-6.

[51] M.L.P. R. Darling, Minimizing mass-transport losses in pem fuel cells, (n.d.) 6074. https://www.electrochem.org/dl/ma/206/pdfs/1933.pdf.

[52] A.H. K. Uda, Z. Noda, K. Sasaki, Electrochemical Characterization of MEAs with Different Pt-loading for the Efficient Use of Pt, ECS Trans. Electrochem. Soc. 80 (2017) 789–799. doi:10.1149/08008.0789ecst.

[53] M.C. Lefebvre, R.B. Martin, P.G. Pickup, Characterization of ionic conductivity profiles within proton exchange membrane fuel cell gas diffusion electrodes by impedance spectroscopy, Electrochem. Solid-State Lett. 2 (1999) 259–261. doi:10.1149/1.1390804.

[54] T. Suzuki, H. Tanaka, M. Hayase, S. Tsushima, S. Hirai, Investigation of porous structure formation of catalyst layers for proton exchange membrane fuel cells and their effect on cell performance, Int. J. Hydrogen Energy. 41 (2016) 20326–20335. doi:10.1016/j.ijhydene.2016.09.078.

[55] V. Yarlagadda, M.K. Carpenter, T.E. Moylan, R.S. Kukreja, R. Koestner, W. Gu, L.

Thompson, A. Kongkanand, Boosting Fuel Cell Performance with Accessible Carbon Mesopores, ACS Energy Lett. 3 (2018) 618–621. doi:10.1021/acsenergylett.8b00186.

[56] Y.-C. Park, H. Tokiwa, K. Kakinuma, M. Watanabe, M. Uchida, Effects of carbon supports on Pt distribution, ionomer coverage and cathode performance for polymer electrolyte fuel cells, J. Power Sources. 315 (2016) 179–191. doi:https://doi.org/10.1016/j.jpowsour.2016.02.091.

SUPPORTING INFORMATION

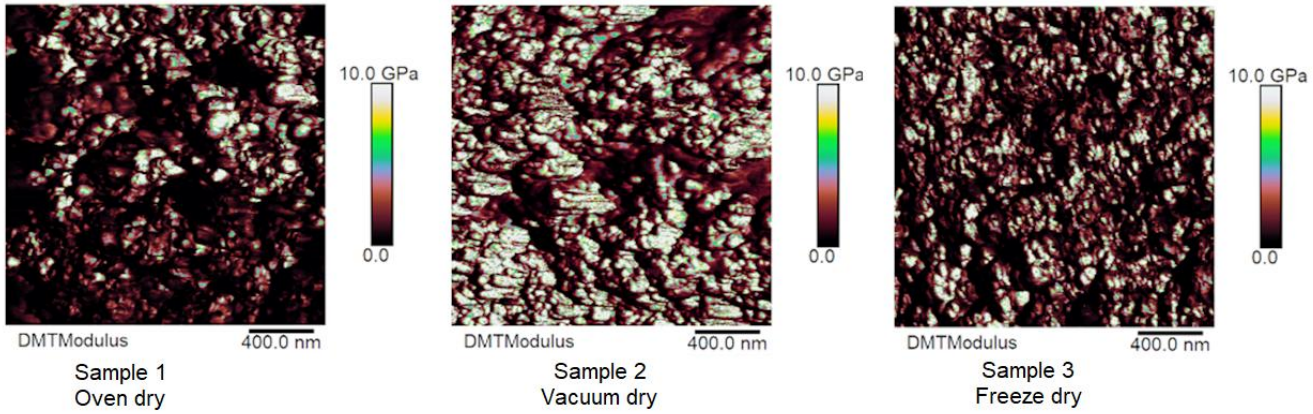

Figure SI 1: a) AFM stiffness measurement by DMT Module

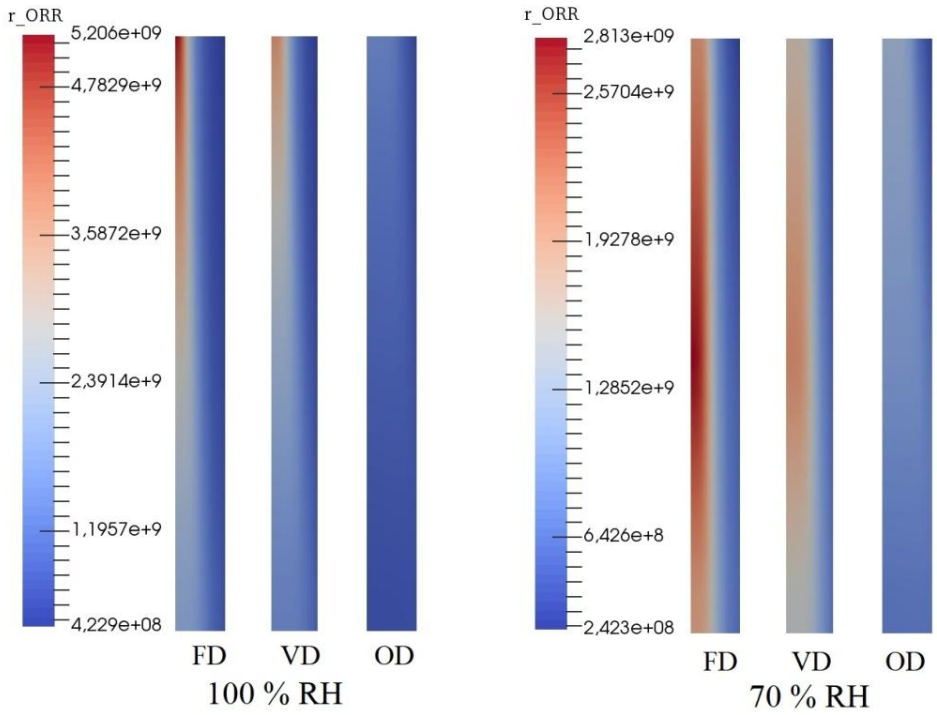

Figure SI 2: The absolute value for the concentration of ORR in both 100 % RH and 70 % RH.

Property	Oven-drying	Vacuum drying	Freeze-drying	Relative error
S_{BET} (m^2 g^{-1}) [a)]	1	6.2	19.6	<5%
Total pore volume (mm^3 g^{-1}) [b)]	103	343.5	635	5-7%
Average pore diameter (nm)[b)]	74	73	106	5-7%
Type of isotherm [a.1)]	IV	II	II	
Porosity (%) [b)]	17	46	59	5%
a) Obtained from BET measurements; [a.1)] from nitrogen physisorption data measurements and in accordance to the IUPAC classification; [b)] From MIP measurements				

Table SI 1: Morphological characterization of Pt/VC-Nafion® powders dried to oven, vacuum and freeze-drying.

Features	100% RH			70% RH		
	FD	VD	OD	FD	VD	OD
OCV (mV)	915	920	928	912	913	926
Potential at 2.5 A (mV)	766	765	777	756	754	768
Potential at 12.5A (mV)	630	609	581	602	585	565
Potential at 25A (mV)	507	462	282	427	386	150

Table SI 2: Average numerical values from the polarization curve of different MEAs prepared from freeze dry (FD), vacuum dry (VD) and oven dry (OD).

Initial variable	Anode	PEM/Anode	Cathode/ PEM	Cathode
P_g	$P_{g,out,anode}$	-	-	$P_{g,out,cathode}$
S_l	0	-	-	0
$x_g^{H_2O}$	$RH_{anode}P_{sat}^{H_2O}/P_g$	-	-	$RH_{cathode}P_{sat}^{H_2O}/P_g$
$x_g^{O_2}$	0	-	-	$0.21(1 - xg,cathodeH2O$
$x_g^{N_2}$	-	-	-	$0.79\,(1 - xg,cathodeH2O$
$x_g^{H_2}$	$1 - x_{g,anode}^{H_2O}$	-	-	0
T	T_{init}	T_{init}	T_{init}	T_{init}
Φ_{ion}	0	0	0	0
Φ_{elec}	0	-	-	$\Phi_{elec,init}$
μ^{H_2O}	-	$RTln(P_{g,anode}^{H_2O}/P_{sat}^{H_2O})$	$RTln(P_{g,cathode}^{H_2O}/P_{sat}^{H_2O})$	-
P^{H_2}	-	$x_g^{H_2}P_{g,anode}$	$x_g^{H_2}P_{g,cathode}$	-
P^{O_2}	-	$x_g^{O_2}P_{g,anode}$	$x_g^{O_2}P_{g,cathode}$	-

Table SI 3: Initial conditions at the interfaces and in the electrodes.

Table 1

Platinum on Carbon black (40 wt.% Pt/VC)	HiSPEC 4000 Powder	0.5 g	Ionomer to Catalyst powder (Pt/VC) mass ratio is 40:60 [30] or Ionomer to carbon (I/C) ratio is 1.13
Ultra-Pure water HPLC grade	Alfa Aesar	3.0 g	
Cyclohexanol 99%	Sigma-Aldrich	4.0 g	
10 wt.% Solubilized Nafion®	Ion Power	3.4 g	

Table 2

Material Components	**Supplier**	**Specifications**	**Function**
Nafion® XL	DuPont	27.94 μm thickness	Electrolyte, membrane
Commercial gas diffusion electrode	Fuel Cells Etc.	0.3 mg cm^{-2} Pt loading	Anode electrode and GDL
Carbon Paper GDL	SGL Carbon GmbH	25 BC non-woven 235 μm thickness	Gas diffusion layer at the cathode side
Ice cube 35 FC-PO 100 **Gaskets**	QuinTech	2× Frame (1.3 cm width), 5×5 cm^2, 0.5 mm thickness	Sealing
Bipolar plates	DLR	Gold coated SS single channel serpentine flow filed	Cell assembly, Gas distribution
Platinum on Carbon (40 wt.% Pt/VC)	HiSPEC 4000 Powder	Vulcan carbon support	Cathode Catalyst
Ultra-Pure water HPLC grade	Alfa Aesar		Solvent for cathode catalyst ink
Cyclohexanol 99%	Sigma-Aldrich		Solvent for cathode catalyst ink
10 wt.% Solubilized Nafion®	Ion Power	Dispersed in water Eq. wt 1100	Ionomer of the cathode catalyst layer

Table 3

Parameters	**Symbol**	**100 %RH**	**70 % RH**
Anode stoichiometry* (H_2)	λ_{an}	1.8	1.8
Cathode stoichiometry* (air)	λ_{ca}	2.7	2.7
Cell temperature	T_{cell}	80° C	80° C
Humidifier temperature	$T_{bubbler}$	80° C	70° C
Anode outlet pressure (absolute)	P_{an}	1.5 bar	1.5 bar
Cathode outlet pressure (absolute)	P_{ca}	1.5 bar	1.5 bar

Table 4

	CCL Thickness, m	ECSA, m^2g^{-1}	Porosity, %
Freeze drying	14.58×10^{-6}	29.16	24
Vacuum drying	12.67×10^{-6}	20.28	21
Oven drying	11×10^{-6}	16.61	18

Table 5

MPL (Permeability, porosity and pore diameter)	
$\mathbf{K}_{MPL}$= 4.0×10^{-15} [m^2]	
$\emptyset_{MPL}$= 0.75	
$r_{pore,\,MPL}$= 45×10^{-9} [m]	
Thermal conductivity(GDL, MPL, CL)	
λ_{GDL}= 0.60 [$Wm^{-1}k^{-1}$]	
λ_{MPL}= 0.33 [$Wm^{-1}k^{-1}$]	
λ_{CL}= 0.3 [$Wm^{-1}k^{-1}$]	
Exchange current density (ORR)	
i^{0}_{ref}= $1.0e^{-4}$ [A m^{-2}]	
CL conductivity	
FD and VD	OD
A= 1.0×10^{-2} [Sm^{-1}]	A= 0.80×10^{-2} [Sm^{-1}]
B= 3.0	B= 3.0
Ionomer film resistance to oxygen transport	
FD and VD	OD
C= 2.5×10^{5} [sm^{-1}]	C= 2.2648×10^{4} [sm^{-1}]
D= 5.0	D= -1.5

Supplementary Information:

Table SI 1

Property	Oven-drying	Vacuum drying	Freeze-drying	Relative error
S_{BET} (m^2 g^{-1}) [a)]	1	6.2	19.6	<5%
Total pore volume (mm^3 g^{-1}) [b)]	103	343.5	635	5-7%
Average pore diameter (nm)[b)]	74	73	106	5-7%
Type of isotherm [a.1)]	IV	II	II	
Porosity (%) [b)]	17	46	59	5%

a) Obtained from BET measurements; [a.1)] from nitrogen physisorption data measurements and in accordance to the IUPAC classification; [b)] From MIP measurements

Table SI 2

Features	100% RH			70% RH		
	FD	VD	OD	FD	VD	OD
OCV (mV)	915	920	928	912	913	926
Potential at 2.5 A (mV)	766	765	777	756	754	768
Potential at 12.5A (mV)	630	609	581	602	585	565
Potential at 25A (mV)	507	462	282	427	386	150

Table SI 3

Initial variable	Anode	PEM/Anode	Cathode/ PEM	Cathode
P_g	$P_{g,out,anode}$	-	-	$P_{g,out,cathode}$
S_l	0	-	-	0
$x_g^{H_2O}$	$RH_{anode}P_{sat}^{H_2O}/P_g$	-	-	$RH_{cathode}P_{sat}^{H_2O}/P_g$
$x_g^{O_2}$	0	-	-	$0.21(1 - xg,cathodeH2O$
$x_g^{N_2}$	-	-	-	$0.79\,(1 - xg,cathodeH2O$
$x_g^{H_2}$	$1 - x_{g,anode}^{H_2O}$	-	-	0
T	T_{init}	T_{init}	T_{init}	T_{init}
Φ_{ion}	0	0	0	0
Φ_{elec}	0	-	-	$\Phi_{elec,init}$
μ^{H_2O}	-	$RTln(P_{g,anode}^{H_2O}/P_{sat}^{H_2O})$	$RTln(P_{g,cathode}^{H_2O}/P_{sat}^{H_2O})$	-
P^{H_2}	-	$x_g^{H_2}P_{g,anode}$	$x_g^{H_2}P_{g,cathode}$	-
P^{O_2}	-	$x_g^{O_2}P_{g,anode}$	$x_g^{O_2}P_{g,cathode}$	-

Figure(s) - provided separately

Click here to download Figure(s) - provided separately: Figure.docx

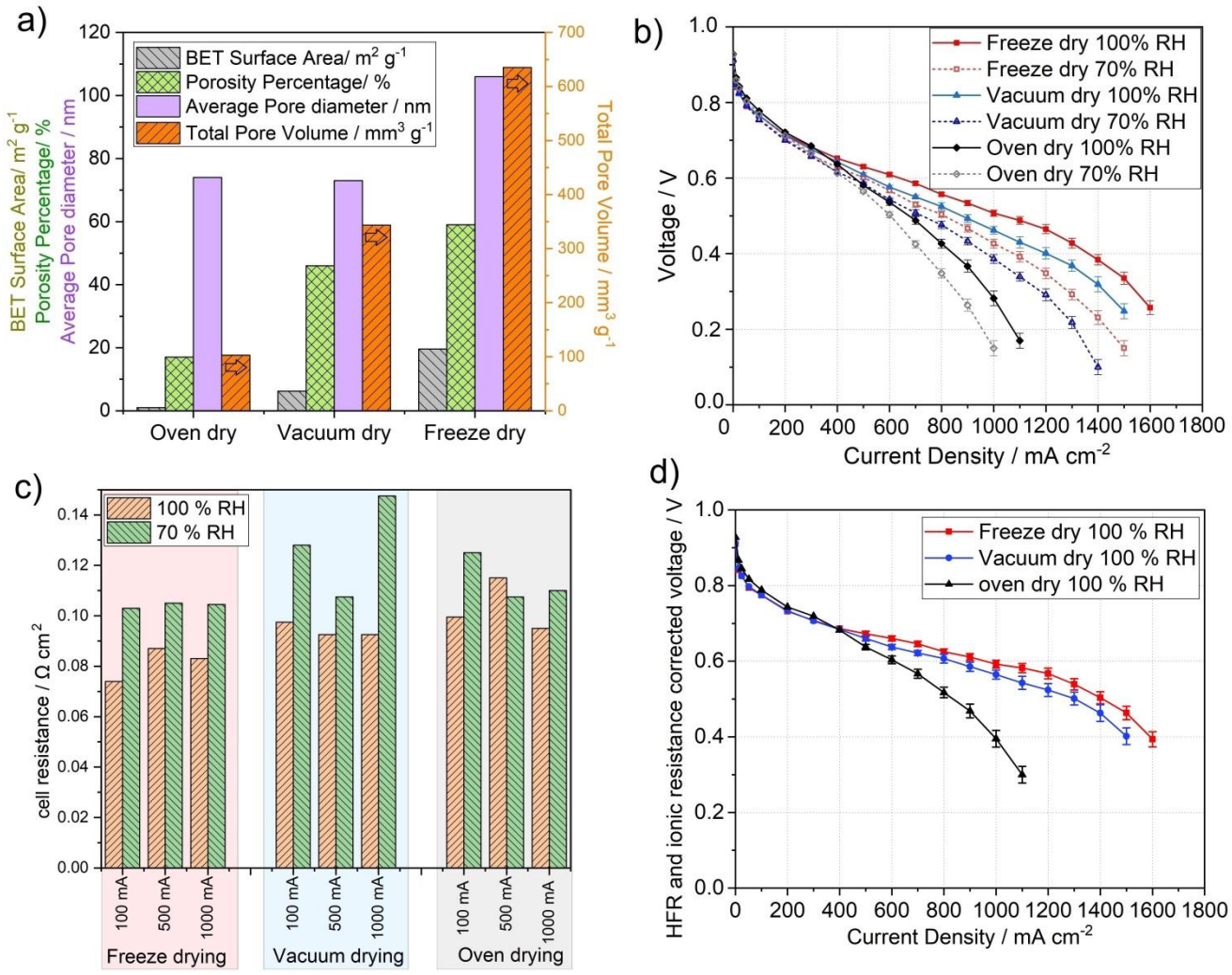

Figure 1

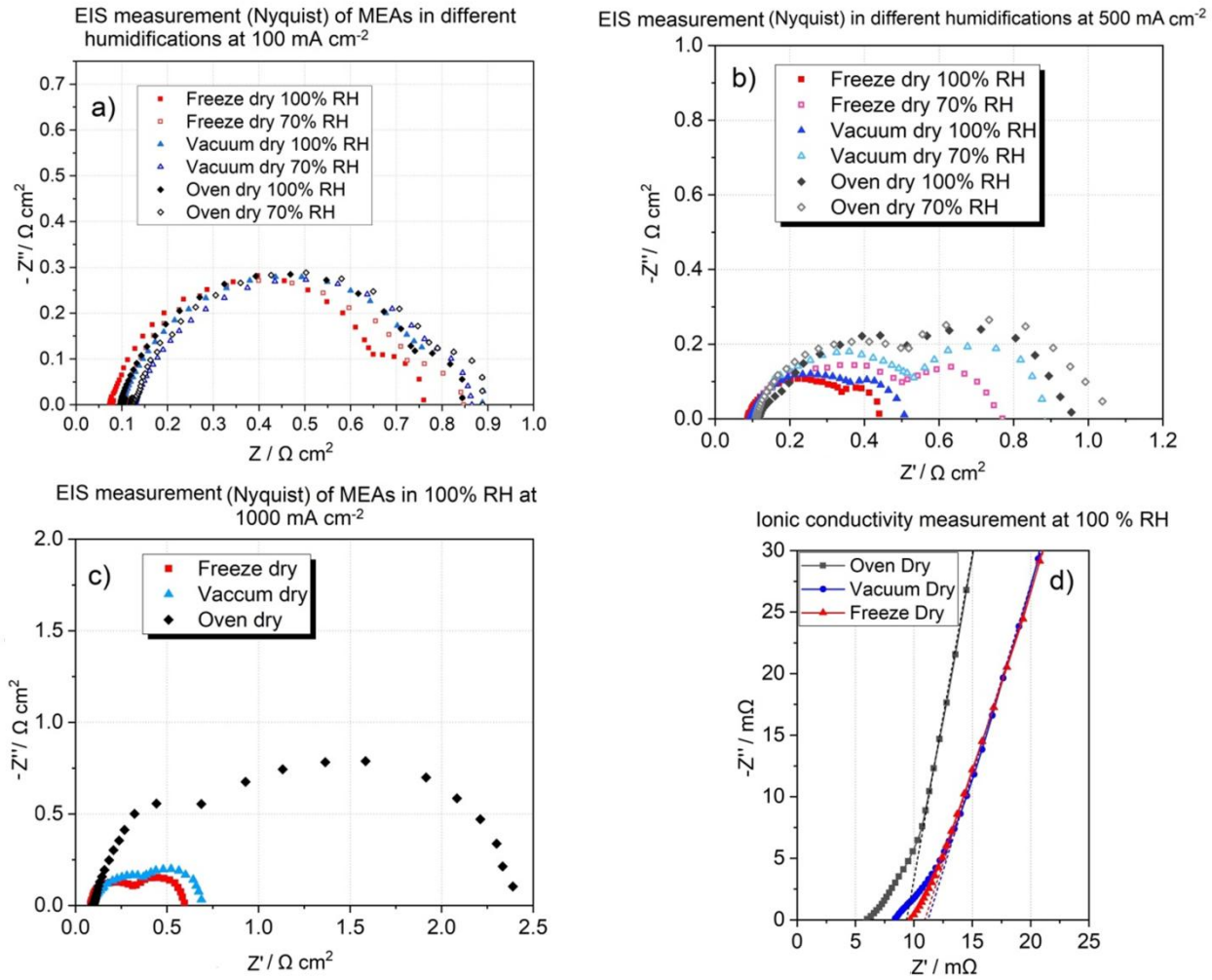
EIS measurement (Nyquist) of MEAs in different humidifications at 100 mA cm-2
a)
Freeze dry 100% RH
Freeze dry 70% RH
Vacuum dry 100% RH
Vacuum dry 70% RH
Oven dry 100% RH
Oven dry 70% RH
- Z'' / Ω cm2
Z / Ω cm2
EIS measurement (Nyquist) in different humidifications at 500 mA cm-2
b)
Freeze dry 100% RH
Freeze dry 70% RH
Vacuum dry 100% RH
Vacuum dry 70% RH
Oven dry 100% RH
Oven dry 70% RH
-Z'' / Ω cm2
Z' / Ω cm2
EIS measurement (Nyquist) of MEAs in 100% RH at 1000 mA cm-2
c)
Freeze dry
Vaccum dry
Oven dry
-Z'' / Ω cm2
Z' / Ω cm2
Ionic conductivity measurement at 100 % RH
d)
Oven Dry
Vacuum Dry
Freeze Dry
-Z'' / mΩ
Z' / mΩ

Figure 2

.

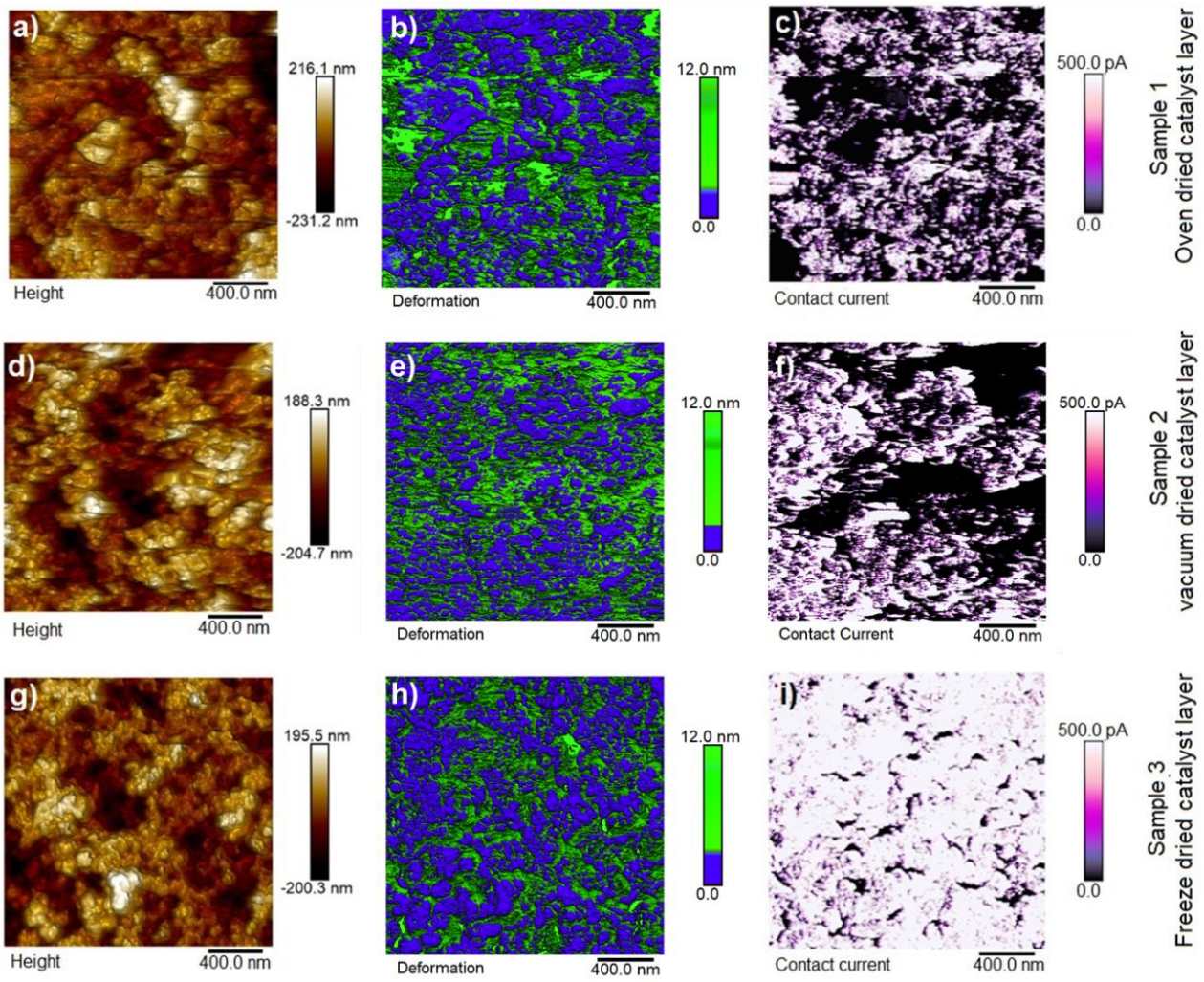
a)
216.1 nm
-231.2 nm
Height
400.0 nm
b)
12.0 nm
0.0
Deformation
400.0 nm
c)
500.0 pA
0.0
Contact current
400.0 nm
Sample 1
Oven dried catalyst layer
d)
188.3 nm
-204.7 nm
Height
400.0 nm
e)
12.0 nm
0.0
Deformation
400.0 nm
f)
500.0 pA
0.0
Contact Current
400.0 nm
Sample 2
vacuum dried catalyst layer
g)
195.5 nm
-200.3 nm
Height
400.0 nm
h)
12.0 nm
0.0
Deformation
400.0 nm
i)
500.0 pA
0.0
Contact current
400.0 nm
Sample 3
Freeze dried catalyst layer

Figure 3

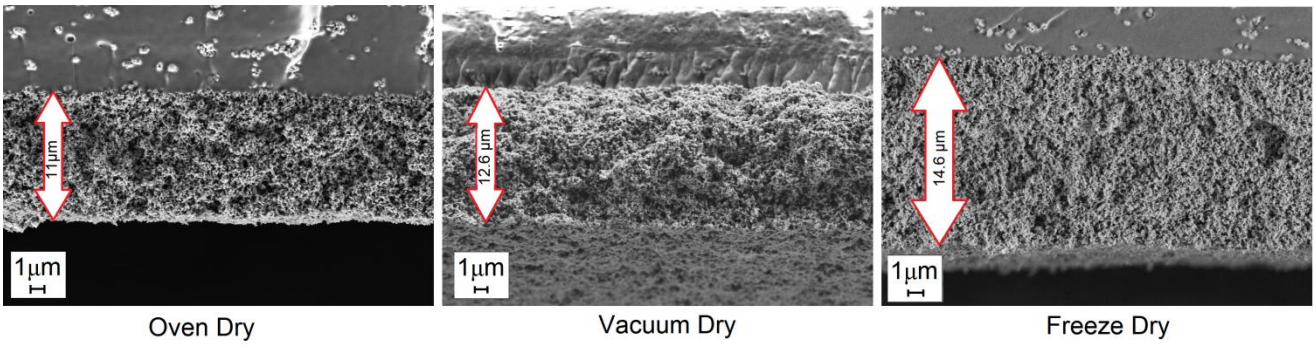

Figure 4

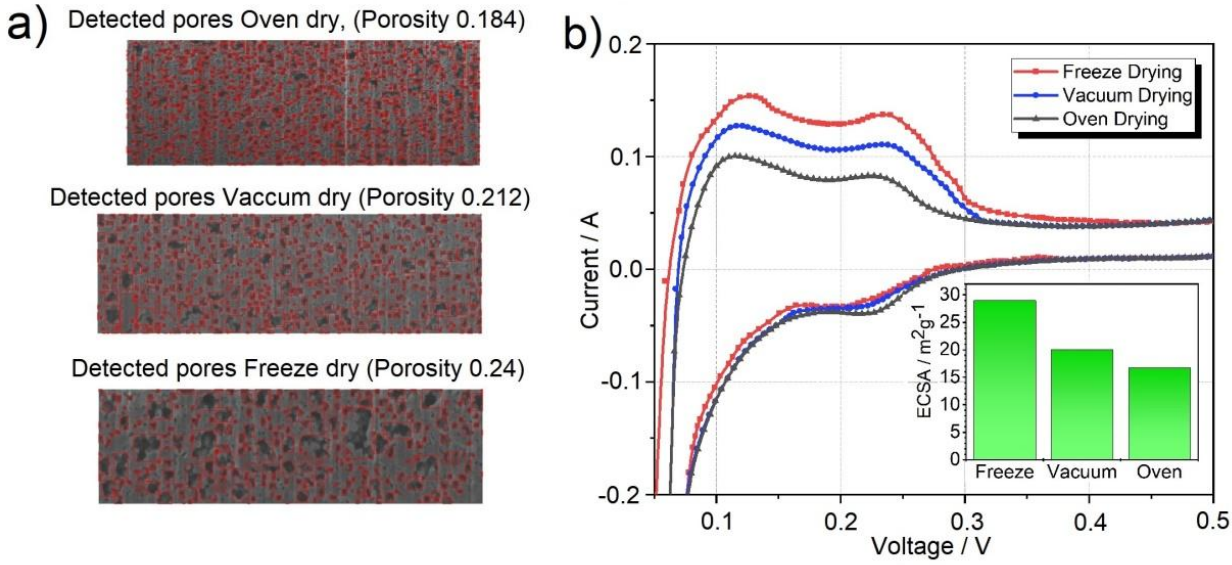

Figure 5

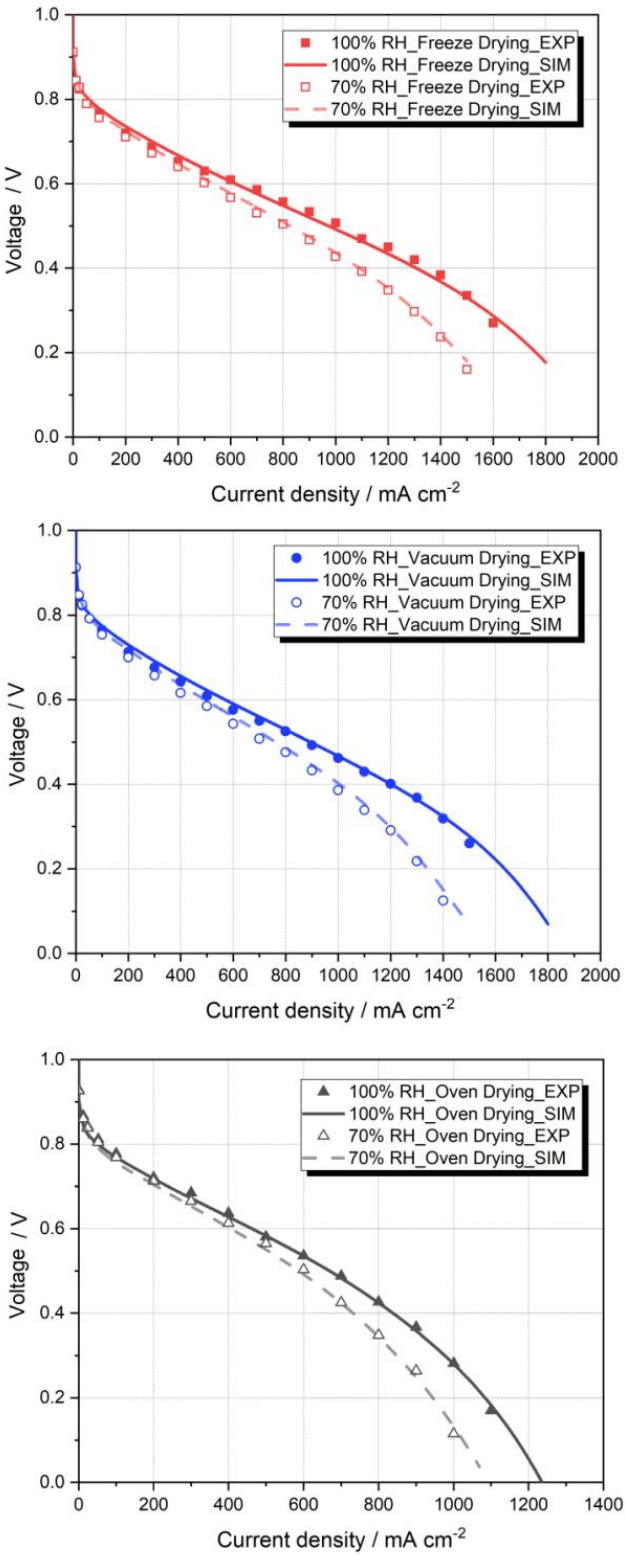
100% RH_Freeze Drying_EXP
100% RH_Freeze Drying_SIM
70% RH_Freeze Drying_EXP
70% RH_Freeze Drying_SIM
Voltage / V
Current density / mA cm-2
100% RH_Vacuum Drying_EXP
100% RH_Vacuum Drying_SIM
70% RH_Vacuum Drying_EXP
70% RH_Vacuum Drying_SIM
Voltage / V
Current density / mA cm-2
100% RH_Oven Drying_EXP
100% RH_Oven Drying_SIM
70% RH_Oven Drying_EXP
70% RH_Oven Drying_SIM
Voltage / V
Current density / mA cm-2

Figure 6

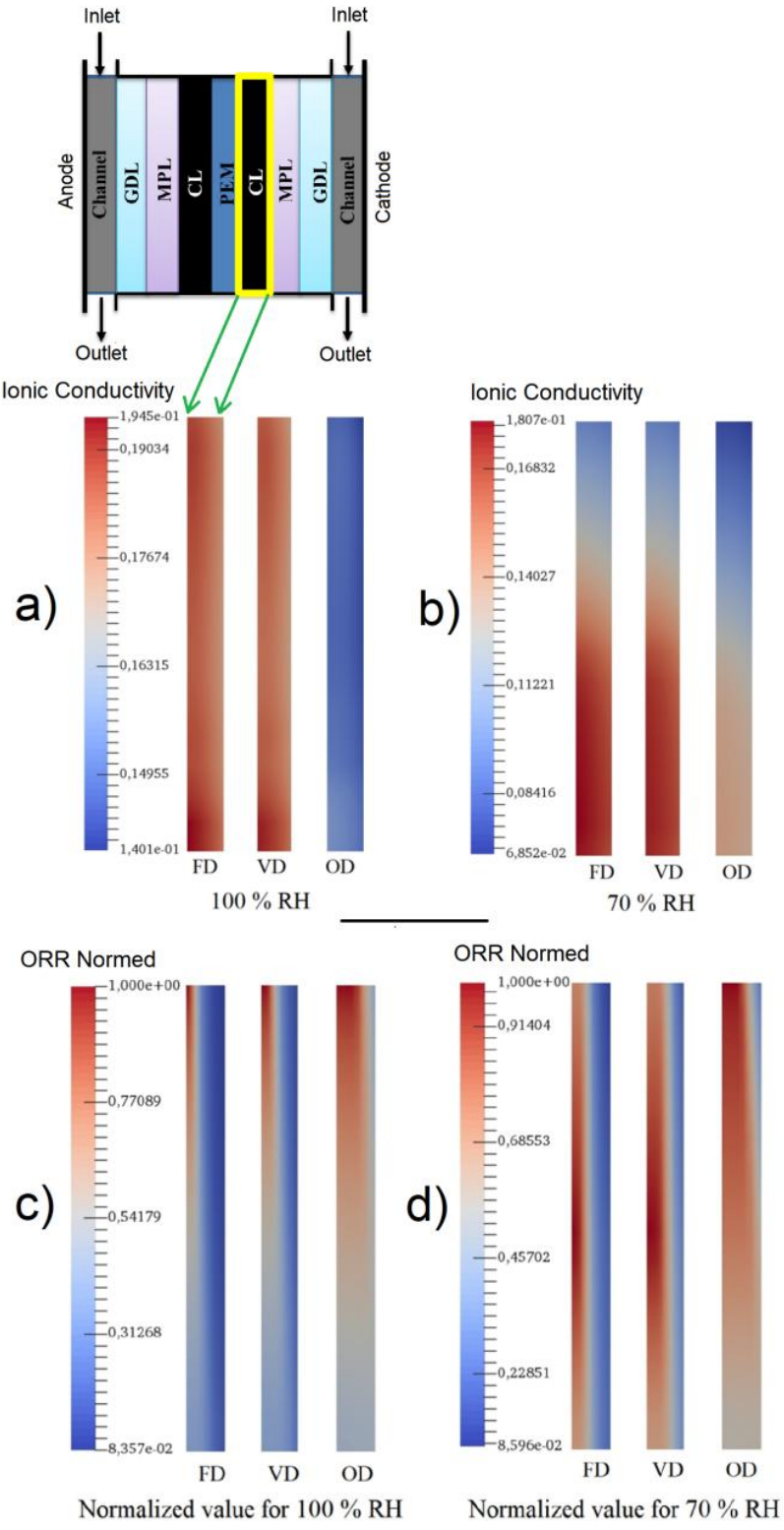
Inlet
Inlet
Anode
Channel
GDL
MPL
CL
PEM
CL
MPL
GDL
Channel
Cathode
Outlet
Outlet
Ionic Conductivity
1,945e-01
0,19034
0,17674
0,16315
0,14955
1,401e-01
a)
FD
VD
OD
100 % RH
Ionic Conductivity
1,807e-01
0,16832
0,14027
0,11221
0,08416
6,852e-02
b)
FD
VD
OD
70 % RH
ORR Normed
1,000e+00
0,77089
0,54179
0,31268
8,357e-02
c)
FD
VD
OD
Normalized value for 100 % RH
ORR Normed
1,000e+00
0,91404
0,68553
0,45702
0,22851
8,596e-02
d)
FD
VD
OD
Normalized value for 70 % RH

Figure 7

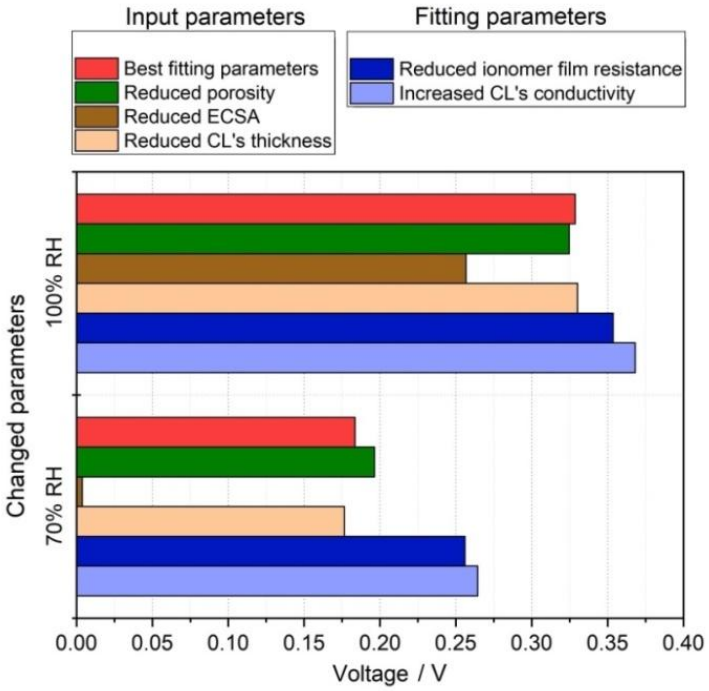
Input parameters
Fitting parameters
Best fitting parameters
Reduced porosity
Reduced ECSA
Reduced CL's thickness
Reduced ionomer film resistance
Increased CL's conductivity
Changed parameters
100% RH
70% RH
0.00
0.05
0.10
0.15
0.20
0.25
0.30
0.35
0.40
Voltage / V

Figure 8

SUPPORTING INFORMATION

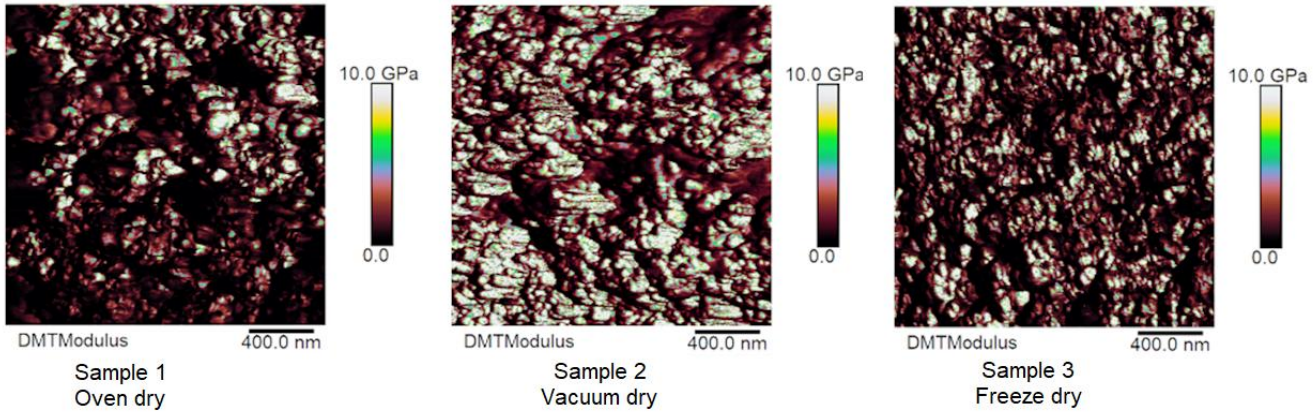

Figure SI 1

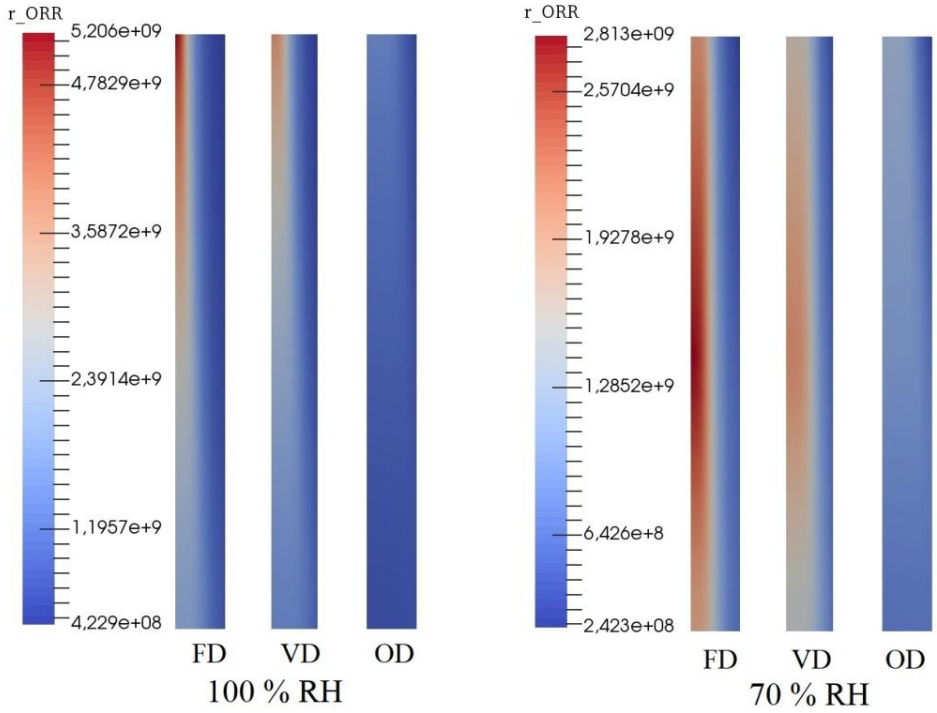

Figure SI 2

Table 1: Specification of the ink formulation for screen-printing coating method.

Table 2: Specification of the materials used to fabricate MEAs for single cell test. ink formulation for screen-printing, and components to assemble.

Table 3: Operating parameters for single cell test bench and the model simulator, (*) the minimum flow was maintained for the test station was for the current density 100 mA cm^{-2}.

Figure 1: a) Morphological characterization of the free standing (non-coated) Pt/ VC/ Nafion® powder shaped by oven, vacuum and freeze drying method. Left-axis exhibits parameters of BET surface area (Grey), porosity percentage (Green), average pore diameter (Purple) and right-axis graph exhibits parameters of total pore volume (orange). ; H_2/ air polarization curves of MEAs with freeze, vacuum and oven dried screen-printed cathode catalyst layers with 0.3 mg cm^{-2} Pt loading at 100% RH (relative humidity) and 70% RH. The temperature was 80 °C with stoichiometric flow and the back pressure was maintained 1.5 bar for both anode and cathode; c) cell ohmic resistance or high frequency resistance (HFR) of three MEAs in different humidification; d) polarization curves with HFR and ionic resistance corrected voltage of the 3 different MEAs in 100 % RH and same condition as Fig 1 b).

Figure 2: Nyquist Impedance spectra a) 100 mA cm^{-2} at 100% RH and 70% RH for three different CCMs dried in three different ways, b) 500 mA cm^{-2} at 100% RH and 70% RH, c) at 1000 mA cm^{-2} only at 100% RH, d) the ionic impedance measurement of 25 cm^2 MEAs at 100% RH (not area normalized).

Figure 3: AFM analysis: a/d/g) height/ topography measurement of three different CL, b/e/h) deformation measurement to ionomer detection, c/f/i) electronic current measurement from three different CL by contact current.

Figure 4: The SEM images from cross-sections of MEAs prepared with different drying techniques.

Figure 5: a) FIB-SEM analysis along with MATLAB image processing applied on the image to measure porosity and pore size distribution, b) Cyclic voltammetry measurement of three different drying techniques including the Pt ECSA values (inset of b). These CLs are compressed to fabricate MEAs.

Figure 6: Fitting of the simulation and experimental polarization curves for three different drying techniques in different relative humidity.

Figure 7: a-b) Ionic conductivity (Sm-1) in CLs due to Freeze drying (FD), Vacuum drying (VD) and Oven drying (OD) techniques in different relative humidity; c-d) ORR rate (Am^{-3}) at 1500 mA cm^{-2} in cathode CLs for freeze drying (FD), vacuum drying (VD) and oven drying (OD) technique for different relative humidity. Normalized values have been plotted to avoid the residual effect of the measurement.

Figure 8: Bar plots emphasizing the influence of input and fitting parameters on the freeze dried MEA (± 25 %) at 1500 mA cm^{-2} in both 100 % and 70 % relative humidity.

SUPPORTING INFORMATION

Figure SI 1: AFM stiffness measurement by DMT Module

Figure SI 2: The absolute value for the concentration of ORR in both 100 % RH and 70 % RH.

Table SI 1: Morphological characterization of Pt/VC-Nafion® powders dried to oven, vacuum and freeze-drying.

Table SI 2: Average numerical values from the polarization curve of different MEAs prepared from freeze dry (FD), vacuum dry (VD) and oven dry (OD).

Table SI 3: Initial conditions at the interfaces and in the electrodes.

Supplementary Materials

Click here to download Supplementary Materials: Supplementary.docx

Credit Author Statement

Krishan Talukdar: *Conceptualization; Data curation; Formal analysis; Investigation; Methodology; Project administration; Supervision; Validation; Visualization.*
Roles/Writing - original draft; Writing - review & editing

Md Asaduzzaman Ripan: *Data curation; Formal analysis; Investigation; Methodology; Software; Validation; Visualization.*

Thomas Jahnke: *Conceptualization; Formal analysis; Investigation; Methodology; Project administration; Resources; Software; Supervision; Validation.*
Writing - review & editing

Pawel Gazdzicki: *Conceptualization; Funding acquisition; Investigation; Methodology; Project administration; Resources; Validation; Visualization;*
Writing - review & editing

Tobias Morawietz: *Data curation; Formal analysis; Investigation; Methodolog; Visualization.*
Writing - review & editing

K. Andreas Friedrich: *Conceptualization; Funding acquisition; Investigation; Methodology; Project administration; Resources; Supervision; Validation; Visualization;*
Writing - review & editing

***Declaration of Interest Statement**

Declaration of interests

☒ The authors declare that they have no known competing financial interests or personal relationships that could have appeared to influence the work reported in this paper.

☐The authors declare the following financial interests/personal relationships which may be considered as potential competing interests: